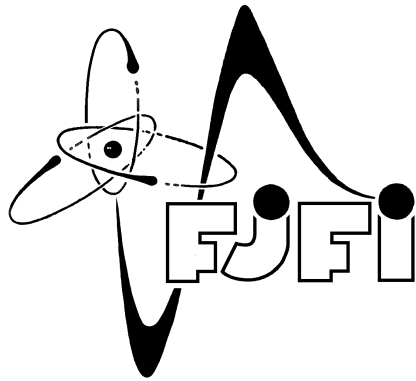**CZECH TECHNICAL UNIVERSITY IN PRAGUE**

Faculty of Nuclear Sciences and Physical Engineering

Department of Physics
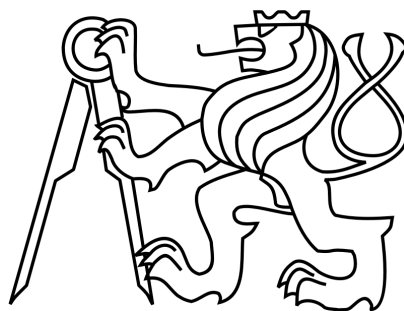
Study of Missing Energy in the Pierre Auger Observatory

Master Thesis

Prague, 2013   Elena Rakovská
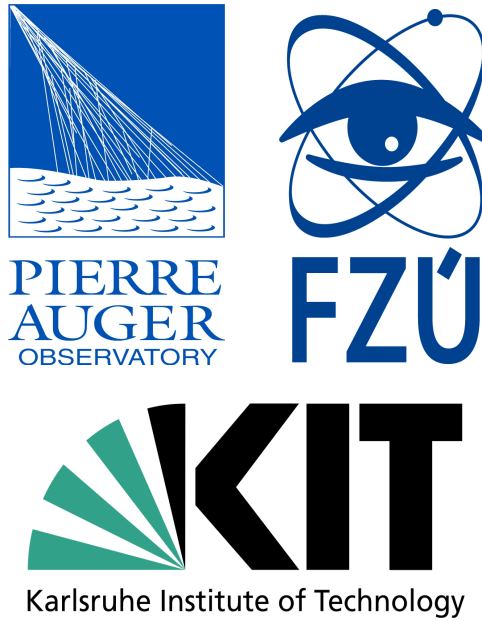
Declaration

Here I declare that I wrote my research project independently and exclusively with the use of quoted bibliography.

I agree with usage of this thesis in accordance with the Act 121/2000 (Copyright Act).

Prague ....

....
Elena Rakovská

Acknowledgement

Elena Rakovská

Title:	**Study of Missing Energy in the Pierre Auger Observatory**
Author:	Elena Rakovská
Field of study:	Nuclear Engineering
Specialization:	Experimental nuclear physics
Type of work:	Master thesis
Supervisor:	RNDr. Jiří Chudoba, Ph.D., Institute of Physics AS CR
Consultant:	Dr. Markus Roth, Institute for Nuclear Physics, Karlsruhe Institute of Technology
Consultant:	RNDr. Petr Trávníček, Ph.D., Institute of Physics AS CR
Keywords:	Pierre Auger Observatory, Missing Energy, Extensive air showers, Cosmic rays, Hadronic models

Abstract: Ultra High Energy Cosmic Rays (UHECR) represent the most energetic source of elementary particles available to scientists. Pierre Auger Observatory (PAO) researches UHECR with unique hybrid detection aperture, a combination of water Cherenkov detectors and fluorescence telescopes. Energy measured with the fluorescence detector must be corrected by the energy of the undetected particles, mostly of neutrinos and high energy muons. At PAO collaboration, a new approach for the determination of the missing energy was presented. It uses a different parametrisation, based on the measured values closely related to the missing energy origin. The novel method was newly applied on data from the Infill array, which is sensitive to the showers with energies down to $\sim 10^{17}$ eV. The missing energy fraction grows with decreasing energy and therefore its estimation plays in the low energy region an important role. Our preliminary results indicate that the missing energy is significantly underestimated by the official reconstruction method. This has a direct impact on the shift of the energy scale.

Contents

Introduction

Research of cosmic rays can be described as a story of scientific adventure. For more than hundred years, scientists are trying to uncover the mysteries of extremely high energetic particles arriving from the universe with measurements on the peaks of mountains, in the hot air balloons and other distant places. Usually the discovery of one secret has generated many new questions that concern astronomers, as well as particle physicists. Since cosmic rays carry information about high-energy processes taking place in their sources and the galactic and extragalactic magnetic fields, the rapidly expanding area of astroparticle physics can clarify different characteristics of the universe.

The main purpose of this work is study the of missing energy in cosmic air showers at low energies at the Pierre Auger Observatory. It is divided into four main parts.

Brief introduction into astroparticle physics is given in the first chapter. Short historical review as well as the most recent opened questions in this field are included.

The second chapter is focused on the experiment at the Pierre Auger Observatory and questions connected with the highest energy cosmic rays. Energy reconstruction and calibration methods are described. Some of the important results from the experiment are introduced.

Missing energy and its determination at the Pierre Auger Observatory is the main topic of the third chapter. It summarises the official reconstruction method as well as an alternative estimation of the missing energy.

Finally, study of the missing energy for Infill array at the Pierre Auger Observatory is the topic of the last chapter. Investigation based on Monte Carlo simulations of extensive air showers is explained. For the final result, the real data are used. The concluding chapter summarises the content of the thesis.

Chapter 1

Cosmic Rays in a Nutshell

Cosmic radiation is one of the most interesting parts of contemporary physics. For more than a century, its observation has raised questions, many of which still remain unanswered. Austrian physicist Victor Hess was the first who was dealing in greater details with particles coming from the universe as early as in 1912. The cosmic rays concept has been introduced by American physicist Millikan in 1925. Hyperbolic interpretation "Things, which are raining from the sky and are not wet" is popular because the correct definition is ambiguous. Cosmic rays are nowadays recognised as primary particles, as well as a cascade of secondary particles reaching the ground. The new point of understanding came later with Pierre Auger and his measurement of coincidental events in different altitudes. An extensive air shower was observed and explained as particle cascade after interaction of very energetic primary particle in the atmosphere. He was the key person in the history of cosmic rays. Also the biggest experiment in this field was named in his honor.

Cosmic rays were for many years the only source of high energy particles. For example the discovery of positron or muon was possible only due to cosmic rays. During the past years, the strong advancement of man-made accelerators starts to dominate with the hunt for the maximum luminosity. But it will never be possible to reach energies, which are a few magnitudes higher, coming from the universe accelerators. Now the new era starts. The connection between precise data from LHC (Large Hadron Collider) and highest energy events from astroparticle experiments is ready to be investigated. Nowadays, the comparison of these two points of view is an unique opportunity for physics.

Although there is much known about the nature and composition of cosmic rays, it still forms many challenging questions. A motivation to investigate cosmic rays remains still the same as hundred years ago. What kind of particles are flying from the universe to the Earth? Where are their sources and what is the acceleration mechanism?
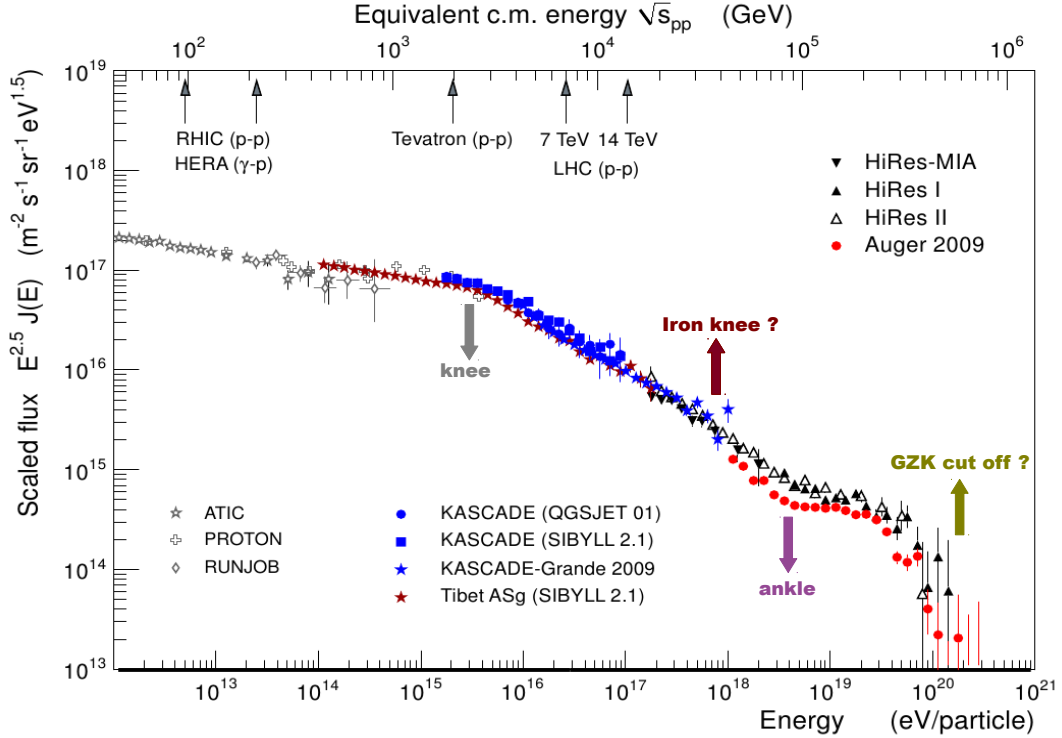
Figure 1.1: Cosmic rays spectrum without mass discrimination composed from different experiments, multiplied by $E^{2.5}$. On the upper axis, energies from collide experiments are denoted for comparison. Taken from [1].

1.1 Energy spectrum of the cosmic rays

There are many astroparticle experiments producing high quality data in the whole range of the energy spectrum, see Fig. 1.1. Cosmic rays with energies lower than 10^{10} eV are coming mostly from the sun and we do not focus on this part of the spectrum. In the energy range $10^{10} - 10^{20}$ eV, the cosmic rays flux follows a power law

$$\phi = \mathrm{d}N/\mathrm{d}E \propto E^{-\alpha}, \tag{1.1}$$

with $\alpha \simeq 2.7$ until PeV energies. This implies we observe one particle per square meter/second in TeV region, but just one particle per km^2 per century! This is the main reason for large areas of astroparticle experiments. There are some typical features of the flux of cosmic rays and the slope is not constant. The first point is so called knee at energies $3 \cdot 10^{15}$ eV, where the flux becomes steeper with $\alpha \simeq 3.1$. An ankle observed by $3 \cdot 10^{18}$ eV brings the spectral index back to the value $\alpha \simeq 2.7$. In between at $4 \cdot 10^{17}$ eV, the second knee is measured ([2]), sometimes called the iron knee.

There are more theoretical predictions interpreting these characteristics of the cosmic rays spectrum. One of the widely accepted idea explains the first knee as a cut-off energy for accelerated protons and light nuclei necessary for the escape from the magnetic field. The escape energy of heavier nuclei is higher (the effect depends

on rigidity) and therefore the second (iron) knee occurs at higher energies. We assume that acceleration mechanism from our galaxy are exhausted at this point and the new increase in ankle suspects extragalactic sources. Further interesting reading to this topic can be found in [3] and [4].

An early idea about acceleration mechanism originates from Enrico Fermi paper, published in 1949 [5]. Energy gain of primary particle is caused by a multiple crossing of a shock wave fronts (e.g. after supernovae explosion) and it is proportional to β (Lorentz velocity). Fermi acceleration of the first order (derived many years after original paper) can not explain energies of primary particles beyond 10^{16} eV. This stays as one of the most interesting unanswered question as well as a discovery of their sources. Classical work dealing with sources, acceleration and propagation of UHECR (Ultra High Energy Cosmic Rays) is [6]. Hot candidates for the source of UHECR are still AGNs (Active Galactic Nuclei). Investigation of pulsars as a source of cosmic rays in the ankle region was presented in the recent publication [7].

One year after discovery of the cosmic microwave background radiation (CMBR), Greisen ([8]) and independently Zatsepin with Kuzmin ([9]) predicted a theoretical limit for energies of UHECR. This GZK cut-off determines $E = 6 \cdot 10^{19}$ eV to be the maximal energy of detected particles. The value is derived as a minimal energy of protons, by interaction with CMBR γ, needed for pion production:

$$p + \gamma_{\mathrm{CMBR}} \longrightarrow \Delta^+ \longrightarrow p + \pi^0$$

$$p + \gamma_{\mathrm{CMBR}} \longrightarrow \Delta^+ \longrightarrow n + \pi^+$$
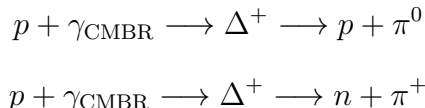
The resulting protons and neutrons loose $\sim 20\%$ of their energy in this process. After propagation through ~ 100 Mpc distance in the universe, protons will have no higher energy than 10^{20} eV [10]. The GZK suppression of the flux should be observed under assumption of proton composition.

There is an serious disagreement in determination of mass composition between two biggest astroparticle experiments: Auger and HiRes [11]. Measurements from the both experiments confirm clearly suppression of the flux of cosmic rays at highest energies, but the shape and position at Auger is different to the GZK one. Auger observes the transition from light to heavy elements at energies above $3 \cdot 10^{18}$ eV. On the other hand, HiRes results fits well to various theoretical predictions about proton spectrum. The true may lay somewhere in between [12], where intermediate mass composition were studied.

1.2   Detection techniques

Detection of cosmic rays is more than one hundred years old. Initially, it started as an attempt to explanation why also strongly shielded ionization chambers have recorded a radiation. Primarily, this was attributed to the residual Earth radiation- so called Erdstrahlung. Finally, the opposite came up true, as it was proven in the science history many times. The radiation was not coming from the Earth, but from the outer space. German physicist and Jesuit priest Theodor Wulf in 1909 came to
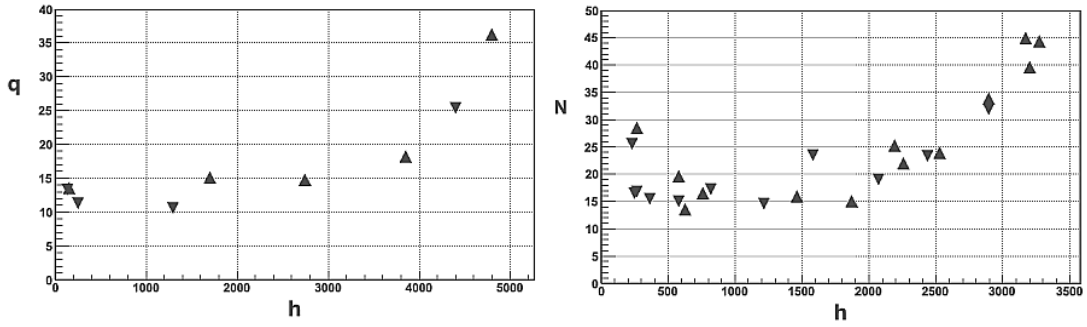
Figure 1.2: On the left side are Hess's results from 1912, on the right are Grygar's measurements from 2006. Value q is in units [ion·cm^{-3}·s^{-1}] and is mean of the air ionization from three electrometers depending on altitude h in [m]. Value N is mean number of detected particles with Geiger-Muller counters in one minute, equally in dependence on h [m]. Direction of the triangles denotes fly-up or fly-down in both graphs. This picture was published in [14].

an interesting conclusion. He based it on radiation measurements at the ground, in the underground caves and on the Eiffel Tower. To his surprise, he discovered with his electrometer that the air conductivity does not drop at all, but tends to rise [13]. Few years later in 1912, Austrian physicist Victor Franz Hess performed revolutionary balloon flight [14]. The beginning of the flight was in Usti nad Labem (in the Czech Republic). It lasted six hours and it was achieved superelevation of 5350 meters. Measurements with three electrometers confirmed an assumption of increasing ionization with hight as the ionization at 4500 meters was twice the value measured on the ground. Hess's interpretation of these results ensues, that sources of the radiation must be searched in the universe. At the beginning, his conclusion was not received well among other physicists. Nevertheless, Victor Hess was awarded for his discovery of cosmic radiation with the Nobel Prize in 1936. About 70 years later, the Czech astrophysicist Jiří Grygar reconstructed the balloon flight, where the measurement with two Geiger-Muller counters confirmed the Hess's experiment. Results of the both flights are presented at the figure 1.2.

One of the first ideas explaining the origin of cosmic radiation came from Robert Millikan. He believed it is the binding energy (in form of photons) from creation of atoms composed from more protons and electrons [1]. But this explanation was disproved by Arthur Compton. The name cosmic radiation was replaced with cosmic rays, despite the later findings in cloud chambers, where mostly charged particles flying from the universe were detected.

Revolutionary discovery in the field of cosmic rays belongs to the French physicist Pierre Auger. He observed a time synchronisation of incoming particles in Geiger-Muller counters with 20 m distance from each other. This brought him to an idea that he was observing secondary particles caused by the same source. Next measurements were carried out in Alps and the same coincidences were confirmed by 200 m distance as well. Pierre Auger derived the energy of primary particles to be 10^{15} eV,

---

[1]Neutron was discovered in 1932, it was unknown at that time.

5

what was a very courageous step in that time [15]. His work was an inspiration for many other researcher to build always larger grids of detectors.

Diverse detection techniques were developed in order to investigate cosmic rays in different energy ranges (Fig. 1.3). The shape of the energy spectrum of cosmic rays gives a certain limitation on its detection. At the lower energies, the flux of the particles is sufficient for direct measurements. Primary cosmic ray can be detected on photographic emulsions or by modern particle detectors in air balloons

Figure 1.3: Detections techniques.

and on boards of satellites. Various ground-based methods were developed for higher energy cosmic rays. The most popular are Cherenkov telescopes, water Cherenkov tanks or scintillators. The youngest detection techniques for very high energy particles are fluorescence telescopes. More about the history, development and experiments in cosmic rays field can be found in [16].
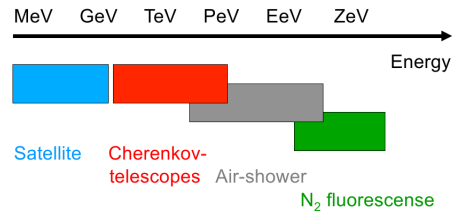
1.3 Extensive air showers

Indirect measurements of cosmic rays with energies above 10^{15} eV are not feasible without understanding of the processes during air shower development. Secondary particles, created in the first interaction, decay or interact further and the shower cascade grows very fast until $X_{\max}$. Extensive air showers are studied with Monte Carlo programs, which utilize different interaction models. Key to understanding of extensive air showers is the modeling of hadronic multiparticle production at energies up to 10^{20} eV, far beyond the reach of accelerator experiments [17].

A standard Monte Carlo simulation program widely used in astroparticle physics is CORSIKA (COsmic Ray SImulations for KAscade) [18, 19]. The most actual version is CORSIKA 7.37xx from April 2013. It can be used for primary particles with energies larger than 10^{12} eV. Two interaction models are required for a simulation. The first one predicts hadronic interaction at higher energies and after reaching a threshold (usually ~ 80 GeV) the computation is based on the second model, for lower energies.

In all high energy models, hadrons are considered as a composition of valence quarks, diquarks, sea quarks and gluons. A color charge is exchanged, when a hadronic interaction occurs. This color connection is described by strings stretched between the partons. The hadronic interaction models used in CORSIKA have very similar basic concepts but there are some differences in the implementation and in fine details [20, 21]. We describe in very simplified way models used in this thesis.

QGSJetII (Quark Gluon String model with JETs) is the new version of QGSJetI with non-linear interactions included. In general, it describes hadronic scattering processes as multiple exchanges of composite objects-pomerons. The model also

allows minijet production for hard diffractive processes and uses Glauber theory for nucleus-nucleus collisions. QGSJetII is the model with least number of free parameters.

EPOS was developed from older model NEXUS. The name is a composition of: Energy conserving quantum mechanical multiple scattering approach based on Parton ladders, Off-shell remnants, and Splitting of parton ladders. EPOS assumes a multiple pomeron exchanges for interactions between hadrons. This model is tuned to describe the largest body of accelerator data by introducing of parameterizations to modify the baseline predictions. The last version, EPOS LHC, was released this year and it was modified with new data from LHC.

SIBYLL 2.1 is the simplest model designed especially for extensive air showers. It contains a minimum of assumptions and differentiates between hadron-hadron, nucleus-hadron, and nucleus-nucleus interactions. In all cases this model relies on fragmented strings. However, SIBYLL can not be used for simulating heavy-ion collisions at accelerator experiments.

Simulation of the PAO detector response, is provided by $\overline{\text{Off}\underline{\text{line}}}$, with input from CORSIKA showers.

CONEX [22, 23, 24] is a combination of Monte Carlo simulation of high energy interactions and fast numerical solution of cascade equations. It is designed for a quick one-dimensional simulation of shower profiles, including energy deposit, charged particles and muon longitudinal profiles. If just a longitudinal profile of the shower is needed, CONEX is a sufficient and much quicker alternative for CORSIKA.

1.4   Toy model of shower development

The earth's atmosphere is in fact a large hadron calorimeter. Disadvantageous, it is neither an usual sampling calorimeter with smart solution for light collection, nor a classical homogeneous calorimeter. That is because the atmosphere's density varies with the altitude. From the other point of view, a very positive attribute is huge size. From the first interaction point the cascade starts to grow till $X_{\max}$ [g/cm^2], the atmospheric depth where the shower reaches maximum number of particles.

To imagine a development of extensive air shower, it is usual to divide it in three components: electromagnetic, hadronic and muons with neutrinos. There are two basics processes in the pure electromagnetic showers: bremsstrahlung and pair production. For the simplicity, there will be $e^{\pm}$ and γ replaced by universal particle of the same type a, see Fig. 1.4.
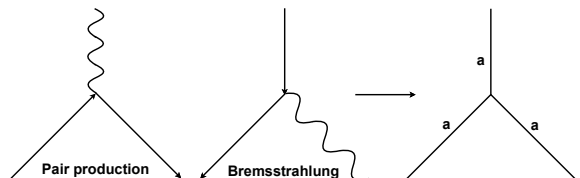

Figure 1.4: Simplified model of electromagnetic shower development.

It will be assumed that every particle decays (with electromagnetic interaction length
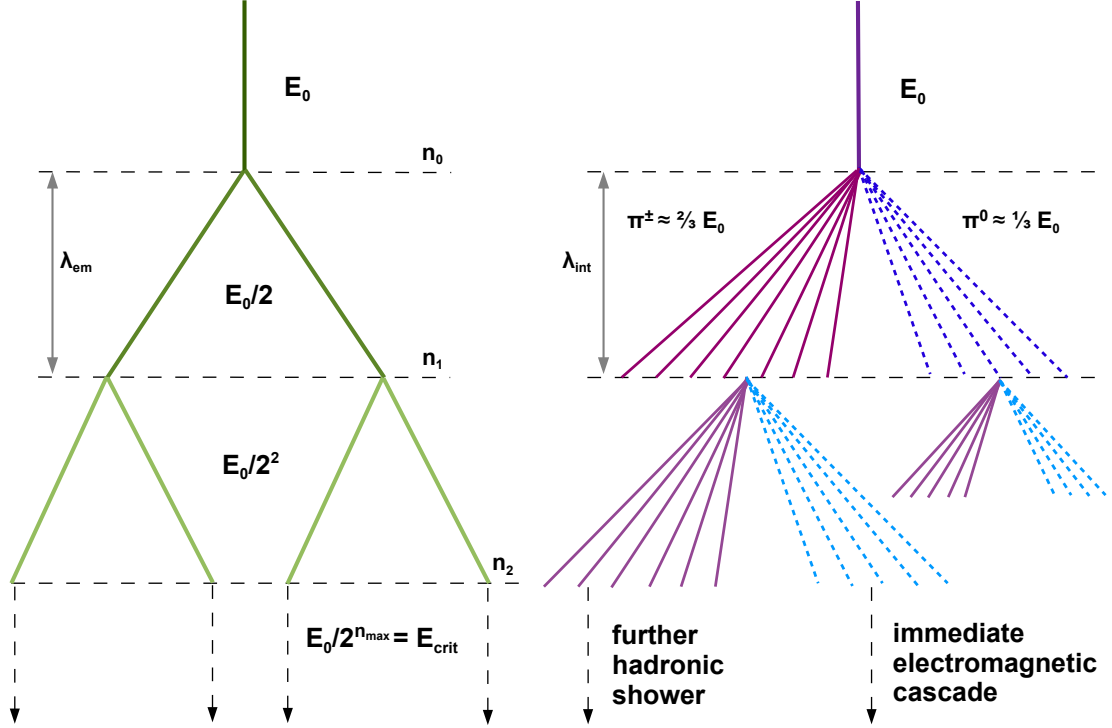
Figure 1.5: Electromagnetic shower development (on the left side) and its expansion to simplified model of hadronic shower cascade.

λ) exactly in two particles with half energy of the mother particle. It means that in the zero generation there is just one particle with energy E_0, in the first generation there are two particles with $E_0/2$, second generation contains 4 particles with $E_0/4 = E_0/2^2$. Generally every particle in the n-th generation has energy $E_0/2^n$. The cascade follows this schema until particles have still enough energy for creating new particles. This energy is called critical energy, in the air $E_{crit} \approx 80$ MeV. When energy jumps below this threshold, competitive processes start to be more important for energy losses, mainly ionization for $e^{\pm}$ and Compton scattering for γ. Maximum number of particles N_{max} occurs in the last generation n_{max} with energy E_{crit}. It means

$$N_{max} = 2^{n_{max}} = \frac{E_0}{E_{crit}} \Rightarrow n_{max} = \log_2 \left(\frac{E_0}{E_{crit}} \right). \tag{1.2}$$

Shower maximum could be now obtained as

$$X_{max} = \lambda \cdot n_{max} = \lambda \cdot \log_2 \left(\frac{E_0}{E_{crit}} \right). \tag{1.3}$$

To describe hadronic component of the extensive air shower in a similar way, it is useful to analyse expansion of the basic electromagnetic shower (Heitler's Model) from Matthews [25]. Lets consider a cascade caused by a single proton, see Fig. 1.5.

In inelastic processes there are equally produced mostly pions, as the lightest mesons. Energy of the primary particle is divided into $\frac{1}{3}$ to neutral pions, which immediately

decay $\pi^0 \to 2\gamma$ and form later electromagnetic component. Remaining $\frac{2}{3}$ of E_0 are taken by charged pions $\pi^\pm$. Total number of particles is $N_{\text{tot}} = N_{\pi^0} + N_{\text{ch}}$ and energy in the n-th generation $E_n = \frac{E_0}{(N_{\text{tot}})^n}$. Analogically to electromagnetic shower, pions produce new generations until they have enough energy. This threshold is called E_{dec}[2], below this energy all particles decay. Charged pions follow mostly the process $\pi^\pm \to \mu^\pm + \overset{(-)}{\nu_\mu}$. Looking at the maximum of the shower, number of charged particles equals to number of muons,

$$N_{\text{max(ch)}} = N_\mu \Rightarrow \log N_{\text{max(ch)}} = \log N_\mu = n_{\text{max}} \cdot \log N_{\text{ch}}. \tag{1.4}$$

Similarly as by the electromagnetic case, the n_{max} can be expressed as

$$\frac{E_0}{E_{\text{dec}}} = (N_{\text{tot}})^{n_{\text{max}}} \Rightarrow n_{\text{max}} = \frac{\log\left(\frac{E_0}{E_{\text{dec}}}\right)}{\log N_{\text{tot}}}. \tag{1.5}$$

Using this expression for the number of muons 1.5

$$\log N_\mu = \log\left(\frac{E_0}{E_{\text{dec}}}\right) \overbrace{\frac{\log N_{\text{ch}}}{\log N_{\text{tot}}}}^{\beta} \Rightarrow N_\mu = \left(\frac{E_0}{E_{\text{dec}}}\right)^\beta. \tag{1.6}$$

Hadronic primaries like protons, α particles and iron nuclei are expected at the highest energies. Considering heavy nuclei as primary with A number of nucleons, the energy E_0 divides equally into each nucleon $E_{\text{nuc}} = \frac{E_0}{A}$. The superposition principle allows to imagine showers caused by heavier nuclei as a sum of A individual proton showers with initial energy E_{nuc}, see Fig. 1.6.

It is exemplary to look how the shower maximum varies with different kinds of primary particles. In the relation 1.3 interaction length will be replaced with elongation

---

[2]In the next chapters E_{dec} is denoted as a critical energy for the pion decay ξ^π_{crit}.
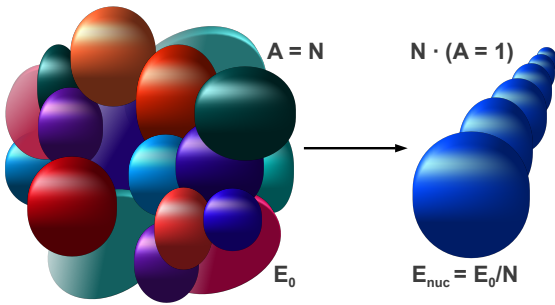

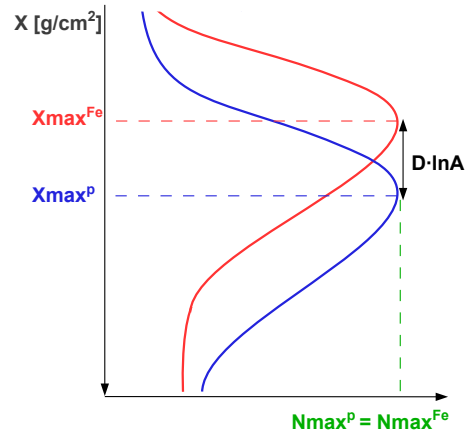Figure 1.6: Superposition principle.

Figure 1.7: Schema of profiles.

rate D_e [g/cm^2] which counts with changing of λ in different altitudes and also $\log_2$ by ln,

$$X_{\max} = D_e \cdot \ln\left(\frac{E_0}{E_{\text{crit}}}\right) \overset{A \geq 1}{=} D_e \cdot \ln\left(\frac{E_0/A}{E_{\text{crit}}}\right) = D_e\left(\ln\frac{E_0}{E_{\text{crit}}} - \ln A\right). \qquad (1.7)$$

It means that a mass sensitive parameter is hidden in the elongation rate inside of $X_{\max}$ because

$$X_{\max}^A = X_{\max}^p - D_e \cdot \ln A. \qquad (1.8)$$

A schematic drawing of this situation is on Fig. 1.7. In the $X_{\max}$ value information about first interaction like cross section, multiplicity and elasticity is hidden.

Similarly from the superposition point of view, it is obvious that the number of particles in maximum is equal for all showers with the same initial energy of nuclei,

$$N_{max}^A = A \cdot \frac{E_0/A}{E_{\text{eff}}} = \frac{E_0}{E_{\text{eff}}} = N_{\max}^p, \qquad (1.9)$$

where the E_{eff} takes into account E_{crit} and also E_{dec}. For a number of muons it is possible to receive an analogical relation to 1.6 for heavier nuclei primaries,

$$N_\mu^A = A \cdot \left(\frac{E_0/A}{E_{\text{dec}}}\right)^\beta = A^{1-\beta}\left(\frac{E_0}{E_{\text{dec}}}\right)^\beta = A^{1-\beta} \cdot N_\mu^p. \qquad (1.10)$$

The number of muons becomes another important mass sensitive parameter.

Another important concept of air shower evolution is so called shower universality. The basic idea assumes that air cascade does not grow any more after reaching its maximum. From this point the shower follows rules of electromagnetism, which are very well understood. It is neglected, how exactly or how fast the shower reaches its maximum. It means that for equally energetic showers observed in the same point of their development (X-$X_{\max}$), the electromagnetic component has the same size for all primary particles. Using this concept, differences between models could be significantly reduced. The same concept does not hold for number of muons, which is strongly correlated with the type of primary particle. Simulated results are shown on Fig. 1.8 and 1.9. The error bars on these plots represent RMS of the distributions of the displayed quantities.
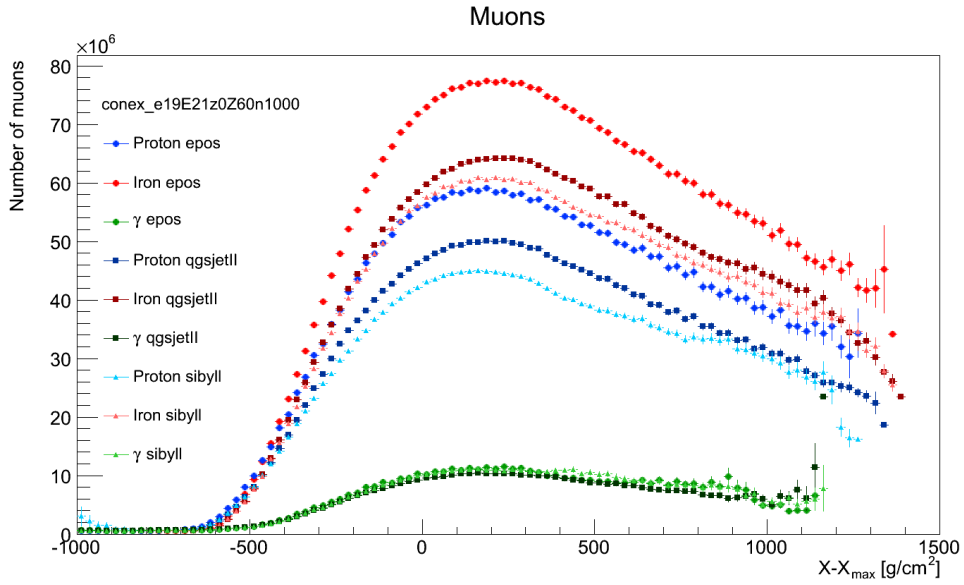
Figure 1.8: Number of muons in dependence to $X - X_{\max}$ for proton, iron and γ showers using three models with energies $10^{19} - 10^{21}$ eV generated with CONEX.
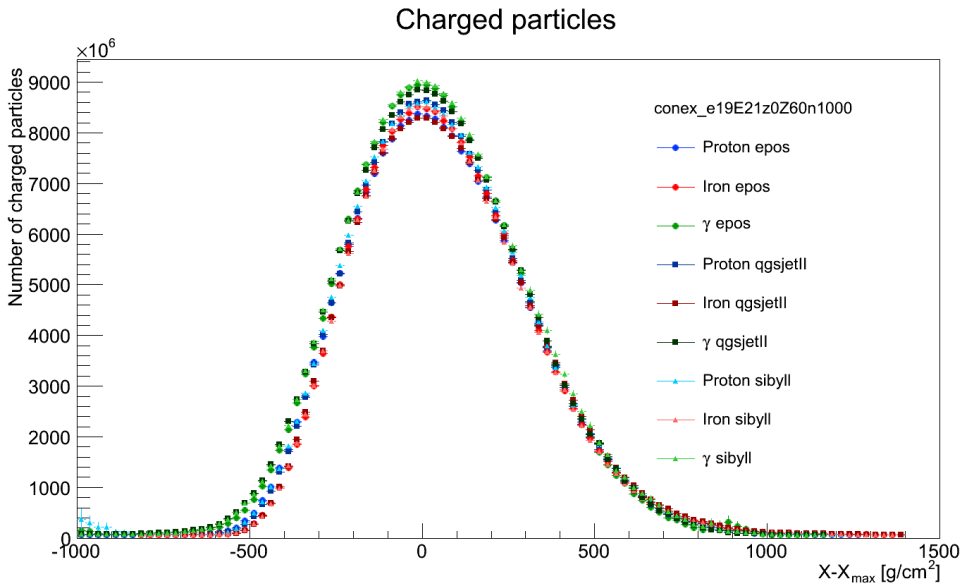

Figure 1.9: Number of charged particles in dependence to $X - X_{\max}$ for proton, iron and γ showers using three models with energies $10^{19} - 10^{21}$ eV generated with CONEX.

Chapter 2

Pierre Auger Observatory

Pierre Auger Observatory (PAO) is the world's leading experiment in the field of ultra high energy cosmic rays (UHECR). It covers the area of 3000 km² in Argentinean plain at altitude 1400 m a.s.l., see Fig. 2.1. It started to collect data in 2004 and the collaboration consists of 17 countries. It is named after the French physicist Pierre Auger and in fact it is attempting to answer the same questions as he was asking many years ago: What kind of particles are hidden in cosmic rays? Where are they coming from? How do they reach their energies?
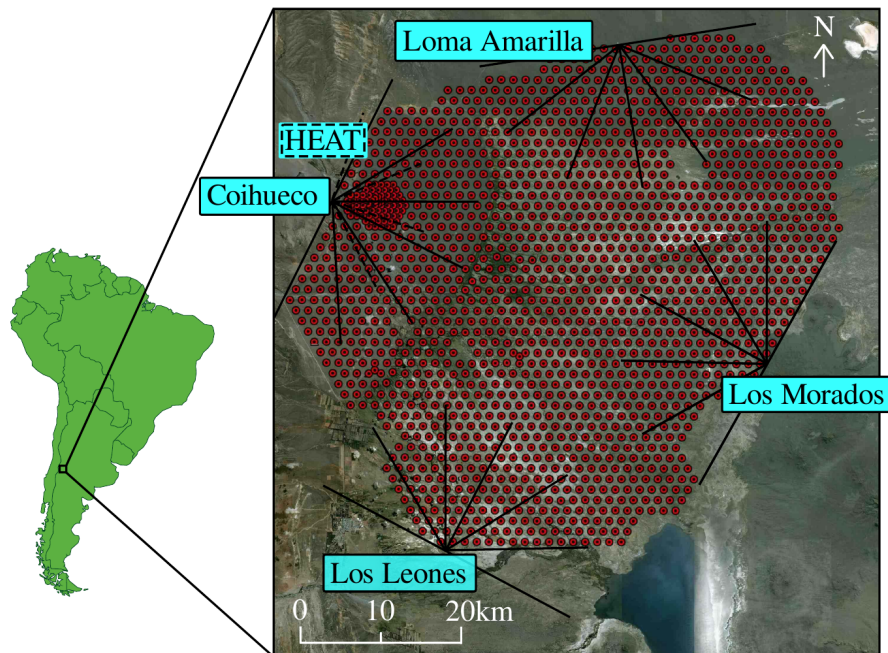

Figure 2.1: Detector layout of PAO near Argentinean city Malargue. Red dots are the Cherenkov water tanks, black lines show field of view of the 24 optical telescopes based in four stations (names in blue boxes). Next to the Coihueco station are three additional high elevation telescopes (HEAT). Dense area shows the AMIGA extension. Taken from [26].

2.1 Hybrid detector

PAO is the first experiment which uses hybrid detection techniques. The surface detector (a principle based on Cherenkov light emission) includes 1600 water tanks with 1.5 km spacing. During clear moonless nights the surface measurement is supported by 24 fluorescence detectors (a principle based on excitation of nitrogen molecules in the atmosphere) placed in four stations at the border of the field. Layout of the detector is shown on Fig. 2.1. $\overline{\text{Offline}}$ is a software framework for analysis of data gathered by the Pierre Auger Observatory, which is developed within the collaboration [27].

Fluorescence detector

Fluorescence detector (FD) at PAO consist of 24 telescopes. Each one is able to cover field of view about $30° \times 30°$ in vertical and azimuthal direction. The fluorescence causes very roughly $3 \cdot 10^9$ [photons/g $\cdot$ cm^{-2}] emitted at $X_{\max}$ for a 10^{19} eV proton shower and the fluorescence photons are distributed isotropically. Data taking is possible only during clear and moonless nights and the duty cycle of FD is therefore only $10-15\%$ of the year. A photo of one fluorescence telescope is shown on Fig. 2.2. After passing a Schott glass filter, there are just photons with wavelengths above 290 and below 410 nm left. Remaining light is corrected in Schmidt optical ring and focused on 3.5×3.5 m^2 segmented mirrors into a 440 pixel (photomultipliers) camera. Light pulses are digitalized in the PMTs every 100 ns. Propagation of the photons in the atmosphere is strong dependent on aerosol content and climatic conditions. At each FD building, there is a LIDAR (LIght Detection and Ranging) facility to estimate the optical depth of the atmosphere during fluorescence measurements. Cloud cameras installed on top of each telescope building are performing a full sky infrared imaging to detect clouds. More informations are available in [28].

Surface detector

One surface detector (SD) consists of $12 \cdot 10^3$ liters of pure water inside of a polyethylene tank. The tank is filled inside with Tyvek liner for high reflection of Cherenkov light, which is registered in three photomultipliers. The tanks are working autonomously due to two solar panels and batteries. For precise time and position information, GPS units and radio transceivers are used. A photo of one SD detector is on Fig. 2.3. Detailed technical information can be found in [29].

Before the data are stored, they have to pass several trigger steps. Each SD station is calibrated in the relative units of vertical equivalent muon (VEM). If the signal gets above the **T1** threshold (1.5 VEM), the data are hold in a local memory for a short time (to be used in case of higher trigger activity). The second signal threshold lies by 3.2 VEM and a **T2** notice is sent to central data acquisition system (CDAS), located in the town of Malargue. Another trigger, Time-Over-Threshold (**ToT**) requires lower minimal signal of 0.2 VEM but for duration for at least 300 ns.
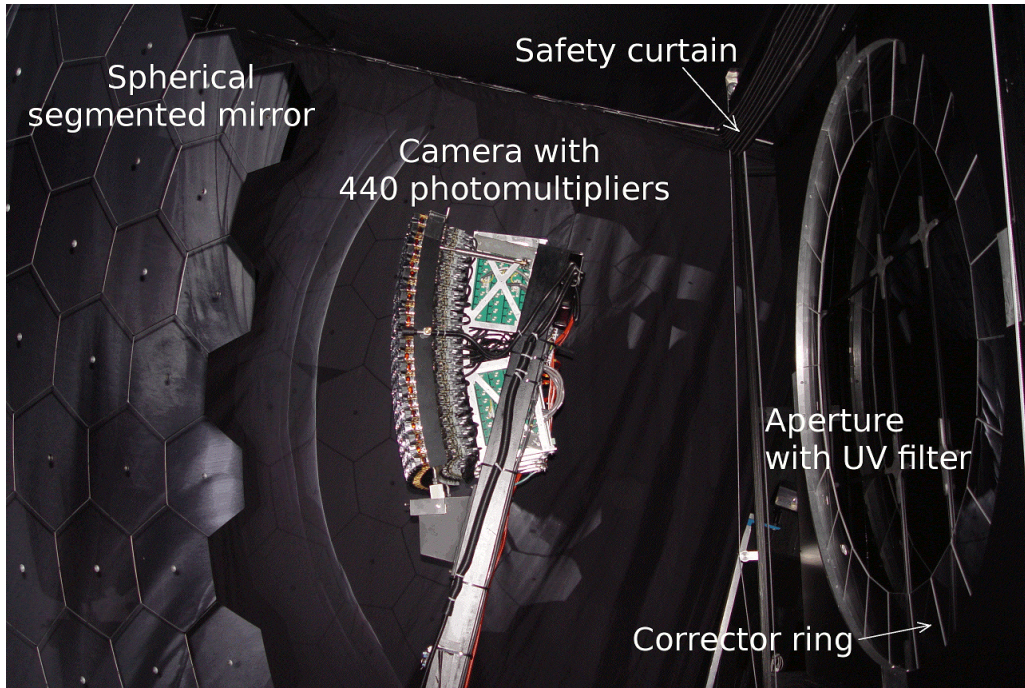
Figure 2.2: Inside view of one telescope from fluorescence detector at PAO. The picture was used in [30].
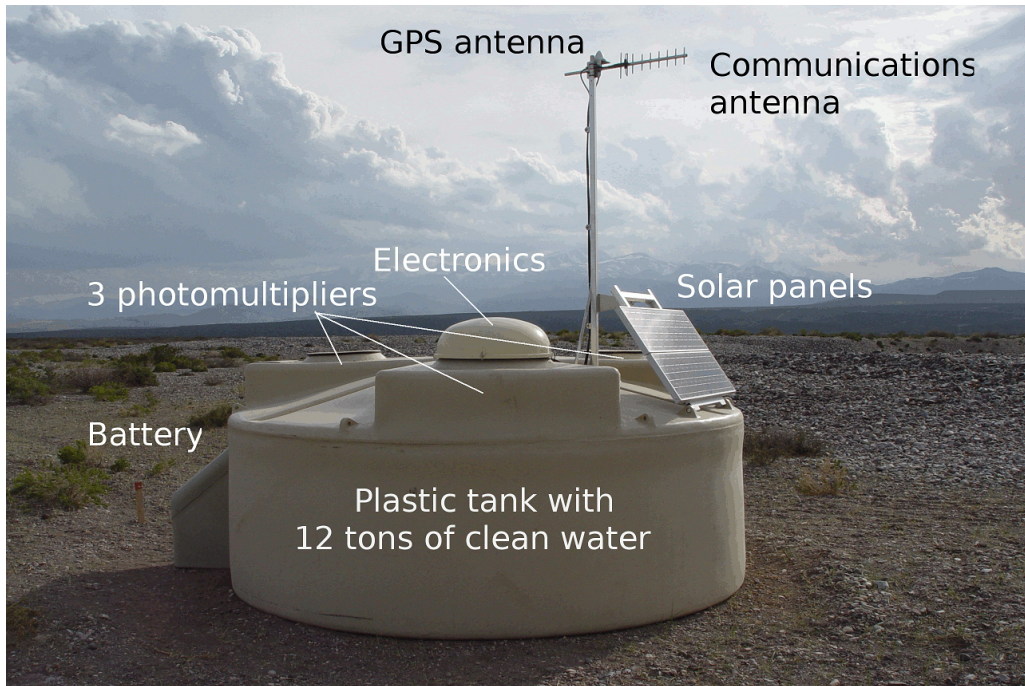

Figure 2.3: One of the water Cherenkov tanks from surface detector at PAO. The picture was used in [30].

ToTd trigger was proposed as an optimisation of the standard ToT trigger to improve the trigger efficiency at low energies. First trigger connecting more station is **T3**, which searches for time coincidence in T2. Physical event trigger **T4** is advanced version of T3 in order to select vertical and horizontal showers. Quality data selection is performed with **6T5** trigger. The necessary condition is fulfilled, when the station with the largest signal is surrounded by six fully functional stations and at least 5 of them are triggered.

2.2 Detector extensions

As mentioned in the previous chapter, the region of the cosmic ray spectrum between $10^{17} - 10^{19}$ eV has a special importance for the discrimination between astrophysical models and determination of the mass composition in the expected transition region from galactic to extragalactic sources. In order to contribute with measurements into this research topic, there are some upgrades and improvements making PAO sensitive to showers with lower energies, next to the basic setup. One of them is AMIGA (Auger Muons and Infill for the Ground Array). Additionally, three telescopes HEAT (High Elevation Telescopes) with higher field of view were build. Another extension is AERA (Auger Engineering Radio Array) using the radio detection principle to measure extensive air showers.

AMIGA consists of a combination of additional water Cherenkov detectors, placed in between the original ones, and a set of muon detectors, each with surface 30 m^2, buried at a depth of 2.3 m (this corresponds to 540 g/cm^2) [31]. The dense array of water tanks, called Infill, is laid out over an area of 23.5 km^2 with 750 m spacing. This allows detection with full efficiency of cosmic rays above $3 \cdot 10^{17}$ eV. Layout with 433 m spacing is planned to cover 5.9 km^2 inside of the Infill and to extend the detectable range down to 10^{17} eV. A prototype of the muon detector consists of 7 buried counters and it is currently in a testing phase. Infill array with 750 m spacing (Fig. 2.4) takes data routinely and the Infill data are analyzed, e.g. in this thesis.

Trigger for Infill events **3ToT** is accepted (with zenith angle $\Theta < 55°$), when at least 3 stations forming a triangle satisfy a local ToT trigger. T4 trigger efficiency model for the Infill array was investigated in [32]. Combination of T4-3ToT requires conditions dependent on primary energy, mass and zenith angle. Therefore the trigger efficiency is defined as:

$$\epsilon = \epsilon(E, A, \Theta) = \frac{\text{number of reconstructed events}}{\text{number of all events}}.$$

This model was used for data selection in this thesis with a cut condition $\epsilon = 0.99$.
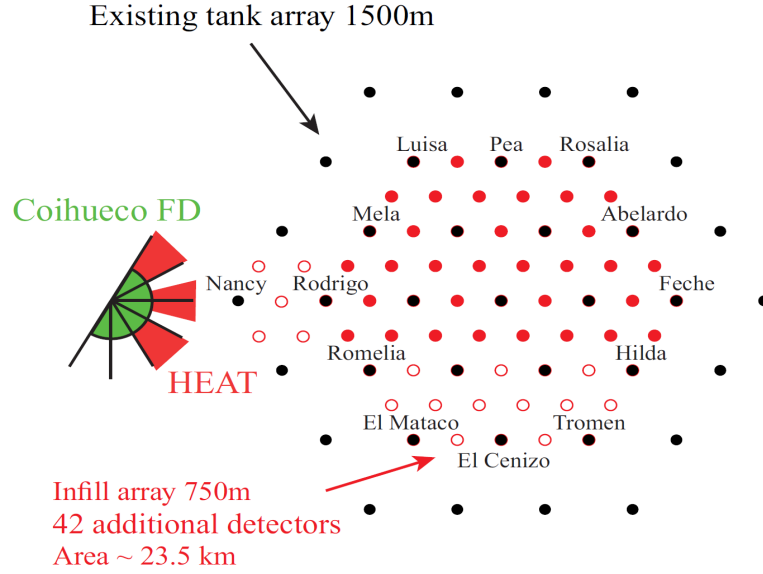
Figure 2.4: Schema of the Infill array, Coihueco and HEAT fluorescence telescopes layout. Black circles stand for water Cherenkov detectors of the regular array, the red ones are added to build Infill array. The figure originate from [33].

HEAT complements the Auger FD with three additional telescopes that are tilted upwards to reach the field of view $30° - 58°$ [33] (Schema on Fig. 2.5). It was designed for fluorescence detection of low energy showers (they develop earlier in the atmosphere ant the X_{max} is higher). HEAT is placed next to the Coihueco station, 6 km away from AMIGA. Due to the connection of both enhancement, PAO disposes with hybrid detection techniques also in the low energy range. The combined HEAT-Coihueco telescope (called HeCo) covers an elevation range from the horizon to $58°$. Visualisation of one HeCo event is depicted on Fig. 2.6.
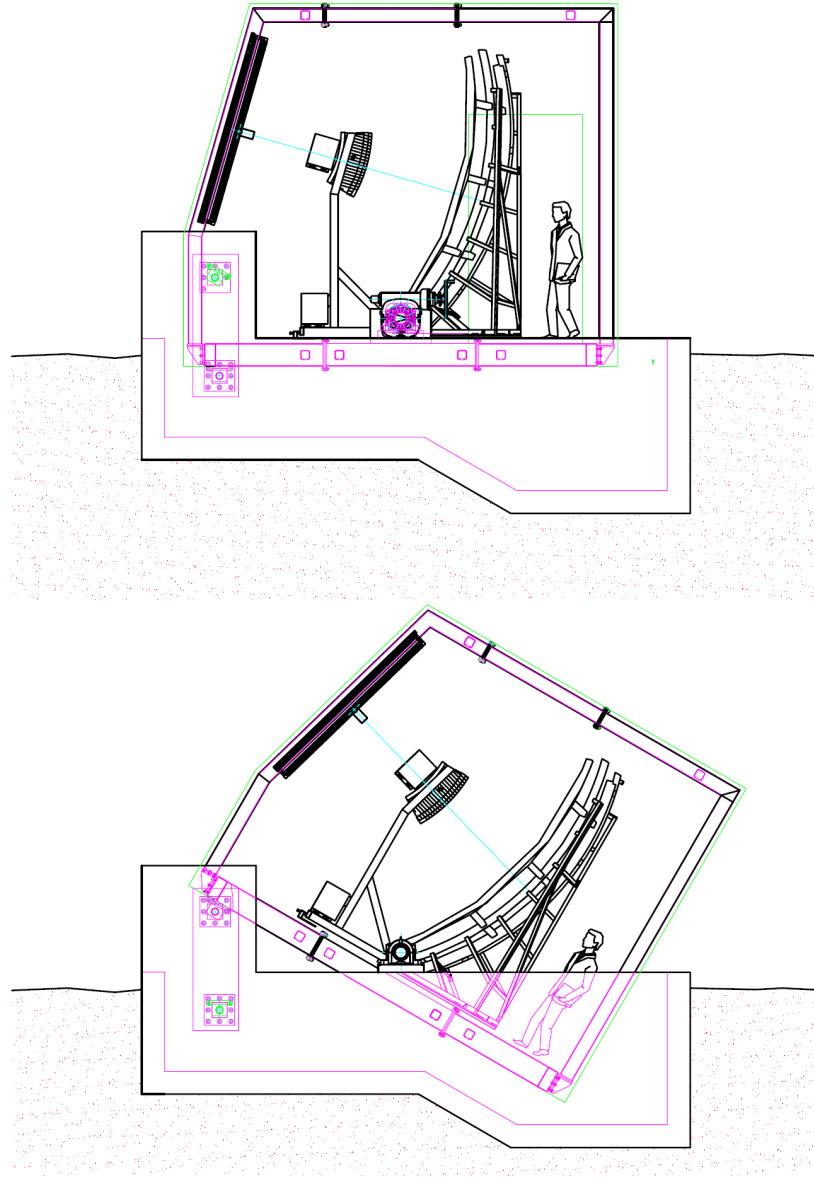
Figure 2.5: Schema of the HEAT telescope. Top: horizontal mode for service and cross-calibration, bottom: orientation for data taking (field of view is higher). From [33].
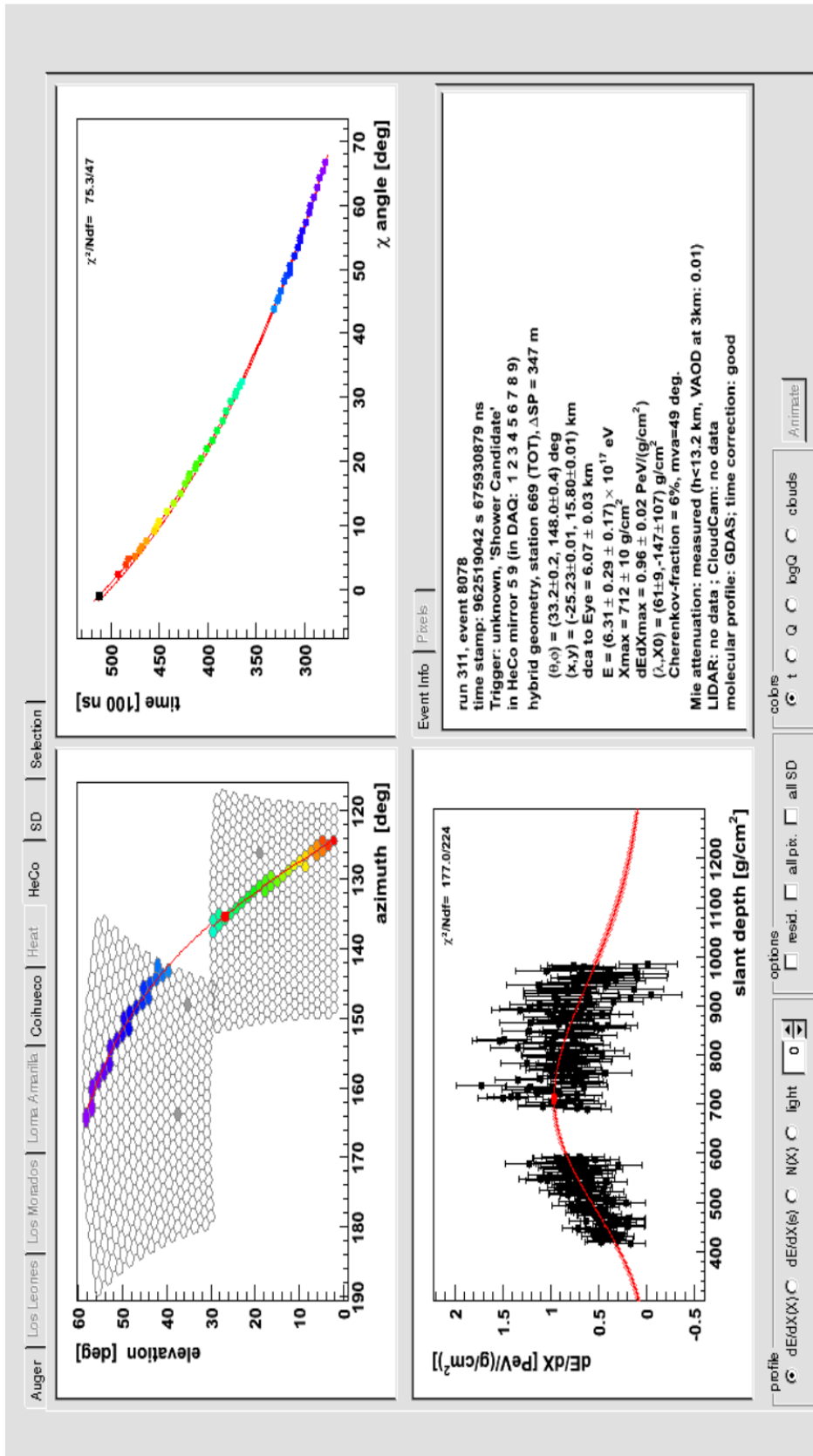
Figure 2.6: One event reconstructed simultaneously with Coihueco and HEAT mirrors (HeCo). The visualization is done with EventBrowser, a tool from official Auger software Offline.

2.3   Energy reconstruction

Two complementary detection techniques (FD and SD) are used at the Pierre Auger Observatory to study extensive air showers initiated by ultra-high energy cosmic rays. From fluorescence measurements, a signal from PMTs is obtained and we need to find a relation to the energy of the primary particle. Similar situation is by SD measurements, where the signal at a fixed distance from the core of the shower is correlated with the primary particle energy.

FD calibration

There are more types of calibrations provided on the fluorescence telescopes [28]. A source of homogeneous light flux placed at the bay entrance is used for one type of absolute calibration. Another method for absolute calibration is based on measurement of nitrogen laser pulses at the distance of 4 km from FD station. Relative calibration with LED and Xenon flash lamps are maintained after every operation night. Big effort is dedicated to atmosphere monitoring. It is necessary to understand the propagation of the fluorescence photons (dependent on climatic conditions) in order to derive a conversion from observed signal to emitted light. The biggest contribution (14%) to overall systematic uncertainty of FD (22%) comes however from the knowledge of the absolute fluorescence yield [34].

SD calibration

The unique hybrid detector at PAO enables to calibrate the surface detectors with FD measurements without using specific hadronic model simulations. A correlation between calorimetric energy obtained from the FD and the signal at 1000 m from shower core recorded by the SD (S_{1000}) is used for the energy calibration [35]. The analysis is based on golden hybrid events data, where an energy estimator can be derived independently from both detectors. The geometry of the shower is reconstructed from arrival times at SD and time information from FD pixels in the first step. In the second step, collected light at FD mirrors is transformed into calorimetric energy. Next, invisible energy (from undetected particles) must be added to the calorimetric energy to obtain the total energy of the primary particle measured by FD (E_{FD}). The main interest of this thesis will be focused on this step. Before comparision with E_{FD}, the signal from the SD must be independent from zenith angle Θ. Therefore S_{1000} is converted to the signal caused by the same shower with $\Theta = 38°$ (S_{38}). This transition is performed with constant intensity curve (CIC):

$$S_{38} = S_{1000}/\mathrm{CIC}(\Theta), \text{where}$$

$$\mathrm{CIC}(\Theta) = 1 + ax + bx^2 \quad \text{with} \quad x = \cos^2(\Theta) + \cos^2(38°).$$

The final energy calibration for SD events is fitted with power-law function:
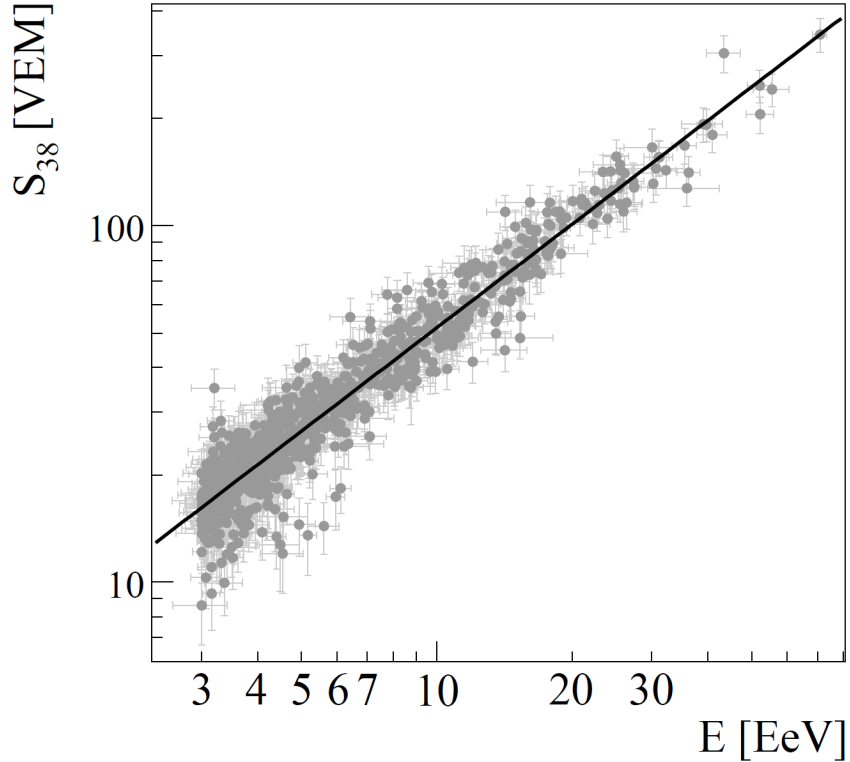
$$E_{\mathrm{FD}} = A \cdot S_{38}^B.$$

Figure 2.7: Correlation between E_{FD} and S_{1000} for 839 high quality golden hybrid events used for the SD energy calibration.

The parameter values presented at the last ICRC ([35]) are $A = (1.68 \pm 0.05) \cdot 10^{17}$ eV and $B = 1.035 \pm 0.009$, see Fig. 2.7.

Energy calibration for the Infill array is analogical. Instead of S_{1000}, the signal at the distance 450 m (S_{450}) is used and for the constant intensity cut the value S_{35} is chosen.

The currently used energy scale at PAO is defined for SD energy spectrum, based on the calibration presented above. The energy scale is still being updated [36]. The recent proposal of the update predicts a positive shift in the energy ($\sim 15\%$) and a significant decrease of the systematic uncertainty. The missing energy contributes to the energy shift with $5\% - 7\%$. If these preliminary results turn out to be correct, it will have important impact on the determination of the energy spectrum, mass composition and many other conclusions.

2.4 PAO results

The Pierre Auger Observatory baseline configuration is complete and is now running smoothly. PAO has collected more data than any other previous experiment and it produces important results in a wide range of astroparticle physics. We selected

just two examples of PAO results connected to determination of mass composition and studies of hadronic interaction. But there are many other interesting results as the energy spectrum, propagation of UHECR, search for the sources, documented elsewhere. Neutrino upper limits comparable to pure neutrion experiments were improved [37].

One of the most common air shower observable is X_{max}. It provides an information about the first interaction and hence about the primary particle type. The mean value of the depth of shower maximum $\langle X_{max} \rangle$ and its dispersion $\sigma(X_{max})$ are often used for the study of the composition of UHECR. The conversion of these values to the mass estimation suffers from the differences within hadronic interaction models and consequently from the different expectations in shower simulations. How can be $\langle X_{max} \rangle$ and $\sigma(X_{max})$ used for interpretation of the mass composition even with uncertainties in the hadronic interaction was presented in [38].

The so called umbrella plots are depicted on Fig. 2.9. These lines define a closed contour that contain all possible combinations of mass mixtures for $A = [0, 56]$. If the cosmic ray composition is any mixture of elements between proton and iron, then the data points must lie within the umbrellas [39]. This is the case just for EPOS interaction model. This disagreement can be explained by the shift of the energy scale.

At Pierre Auger Observatory, it is possible to determine proton-air (after calculation also proton-proton) cross section at center of mass energy $\sqrt{s} = 57$ TeV [40]. For this purpose, the tail of the X_{max} distribution is analyzed. Comparision to the results from LHC experiments are shown on Fig. 2.8.
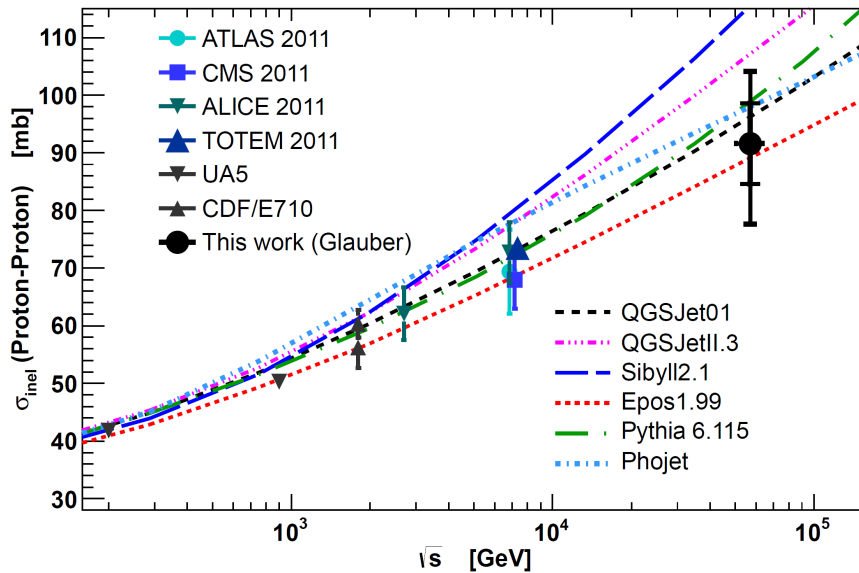
Figure 2.8: Proton-proton cross section calculated from PAO data compared to the results from accelerator experiment. Additionally the comparision to the model predictions. Taken from [40]
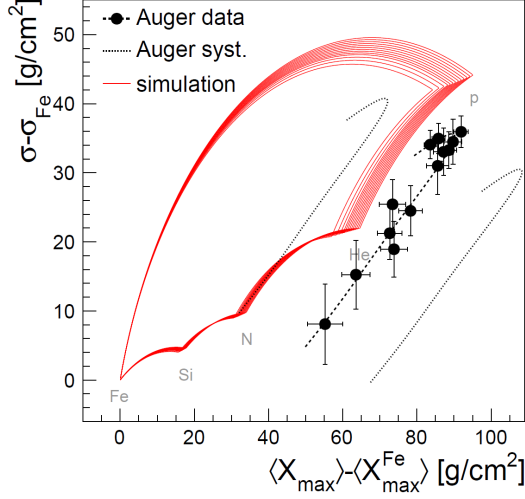
(a) QGSJet01
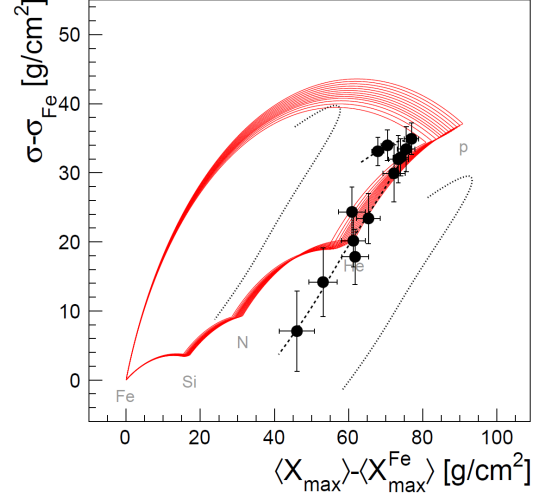
(b) QGSJetII
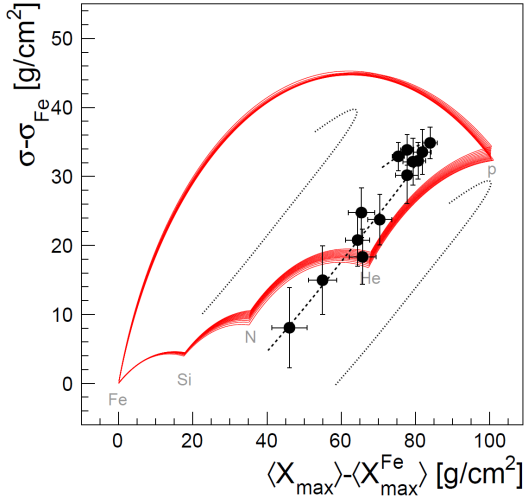
(c) Sibyll2.1
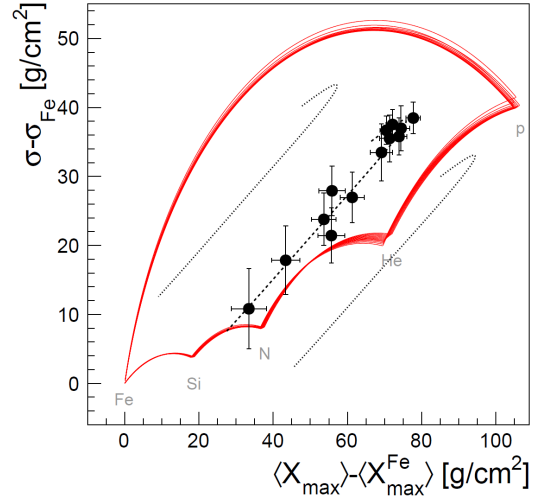
(d) Epos1.99

Figure 2.9: Auger data compared with the average shower depth and its fluctuations with different air shower simulations. The energy of the data points increases from top to bottom (indicated by the dashed line). The figure was published in [39].

Chapter 3

The missing energy of cosmic ray air showers

This chapter deals with problematics of an invisible part of the primary energy, the so called missing energy. This energy is carried away by particles that do not deposit energy in the atmosphere. We describe the standard and an alternative determination of the missing energy.

Every calorimetric detector deals with energy losses. The atmosphere is also a calorimeter, but unfortunately it is not feasible to apply a direct calibration. There is no beam of particles with fixed ultra high energies at the top of the atmosphere. The response of the atmosphere is determined without knowing the exact primary particle energy. That is why the missing energy can be estimated only indirectly.

The shower profiles are inferred from measurement of the fluorescence light with telescopes. The parametrization of the profile $\mathrm{d}E/\mathrm{d}X$ is performed with a Gaisser-Hillas function [41]

$$f_{\mathrm{GH}}(X) = \frac{\mathrm{d}E}{\mathrm{d}X}(X_{\mathrm{max}}) \left(\frac{X - X_0}{X_{\mathrm{max}} - X_0} \right)^{\frac{X_{\mathrm{max}} - X_0}{\lambda}} e^{\frac{X_{\mathrm{max}} - X}{\lambda}}. \tag{3.1}$$

The energy reconstruction of a primary particle could be obtained by integrating the profile, leading to calorimetric energy

$$E_{\mathrm{cal}} = \int_0^\infty f_{\mathrm{GH}}(X)\mathrm{d}X. \tag{3.2}$$

Due to the shower development involving hadronic interactions, a part of the energy is carried away by neutrinos and energetic muons. These particles are invisible for fluorescence detectors and are described as the missing energy E_{miss}. The energy of the primary particle is given by $E_0 = E_{\mathrm{cal}} + E_{\mathrm{miss}}$, with two unknown quantities E_0 and E_{miss}.

Until now, there are two basic approaches to solve this problem. On one hand, the missing energy could be expressed as a function of calorimetric energy and each shower with equal E_{cal} would correspond to the same E_{miss}. On the other hand, missing energy can be computed from different measured quantities and obtained individually for each shower.

3.1 Determination of the missing energy

The standard determination of the missing energy was investigated by Barbosa et al. in [42]. Using Monte Carlo simulations, E_{miss} is represented as a function of E_{cal}. This method is currently used in the official reconstruction of the data from the Pierre Auger Observatory. It is based on CORSIKA code, which allows to track different types of particles[1] at various stages of shower development. The energy of the primary particle at depth X is assumed to be

$$E_0 = \sum_{i=em,had,\mu,\nu} F_i(X) + \sum_{i=em,had,\mu,\nu} D_i(X),$$

where F is the energy carried by particles and D is the energy put into ionization. We must consider the fact that particles in the cascade undergo energy and angle threshold cut. Those which energy is below the threshold, are dropped out from further simulation steps. CORSIKA counts their energy as dissipated. Indeed, a fraction f_i of the energy causes ionization and the rest $(1 - f_i)$ contributes to the missing energy. Neutrinos are added to the invisible energy as soon as produced. At the observation level, electromagnetic particles and a part of the hadronic component are added to the calorimetric energy, whereas muons are added to the missing energy. Taking all these effects into account, E_{miss} shows a small ($<1\%$) dependence on zenith angle but there is a significant difference ($\sim 5\%$) between proton and iron primaries at $E_{\text{cal}} = 10^{18}$ eV. This spread can grow when considering different hadronic models, but in general it decreases at higher energies. The parametrisation used for the reconstruction of data was chosen from a mixed composition of 50% proton and 50% iron primaries with zenith angle $\Theta = 45°$. The functional form is

$$\frac{E_{\text{miss}}}{E_0} = 1 - \frac{E_{\text{cal}}}{E_0} = a + b \cdot (E_{\text{cal}}/\text{EeV})^c. \tag{3.3}$$

The integral of the calorimetric energy as stated in Eq. 3.2, can be solved [43] after substituting $t = \frac{X - X_0}{\lambda}$ and $s = \frac{X_{\text{max}} - X_0}{\lambda}$ in the Gaisser-Hillas function:

$$E_{\text{cal}} = \lambda \frac{\mathrm{d}E}{\mathrm{d}X}(X_{\text{max}}) \left(\frac{e}{s}\right)^s \Gamma(s + 1),$$

where Γ stands for the Gamma function[2]. Part of this equation can be replaced with the expression

$$\frac{\mathrm{d}E}{\mathrm{d}X_{\text{max}}} = f_{\text{GH}} \left(\frac{e}{s}\right)^{-s} t^{-s} e^t.$$

The profile of shower development is fitted with modified a Gaisser-Hillas function, where E_{cal} is a free parameter:

$$f_{\text{GH}} = \frac{E_{\text{cal}}}{\lambda} \cdot \frac{e^{-t} t^s}{\Gamma(s + 1)}. \tag{3.4}$$

---

[1] Particles are divided into four main groups: *em* for electromagnetic component, *had* for hadronic component, μ for muons and ν for neutrinos.

[2] The property of the gamma function $\frac{\Gamma(b+1)}{a^{b+1}} = \int_0^\infty t^b e^{-at} \mathrm{d}t$ was used.
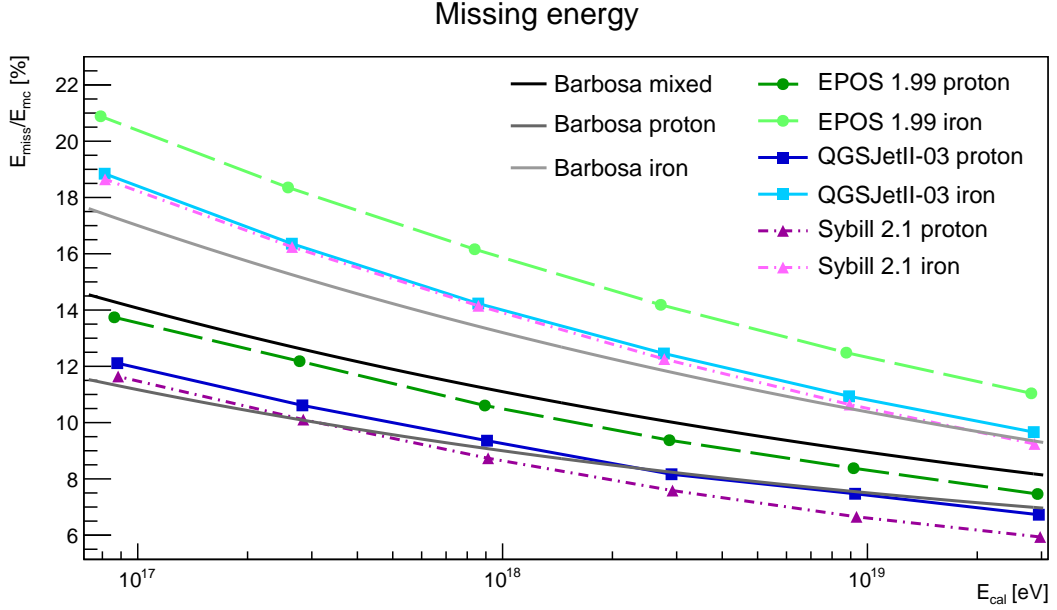
Figure 3.1: E_{miss} as a function of E_{cal} (logarithmic scale on x axis) with three interaction models, for proton and iron primaries, with fixed zenith angle $\Theta = 38°$. Barbosa parametrization (presented in [42]) is included for proton, iron and mixed (50% proton and 50% iron nuclei) composition with zenith angle $\Theta = 45°$.

Since E_{cal} can be obtained from longitudinal shower profile, the missing energy $E_{\text{mis}} = E_0 - E_{\text{cal}}$ can be calculated shower by shower in Monte Carlo simulations from the fitted Gaisser-Hillas function. This approach is to some extend independent on Barbosa calculation. In Figure 3.1 the results of the dependence of E_{miss} on E_{cal} obtained from CONEX simulations compared with the Barbosa parametrization (Eq. 3.3) are presented. The calorimetric energy was obtained from a fit of Eq. 3.4. The missing energy was computed as difference to the Monte Carlo energy of the primary particle. Each marker represents the average of thousand showers with fixed zenith angle $\Theta = 38°$ and six different energies from 10^{17} to $10^{19.5}$ eV with half decade steps. The lines are just connecting markers of proton or iron primaries within one interaction model for illustration.

The size of the missing energy is strongly related to the hadronic interaction models. The number of pions generated by collisions determines the amount of muons, neutrinos and the size of the electromagnetic component. E_{miss} can be expressed as a function of multiplicity N_{ch}, as derived for example in [44]:

$$\frac{E_{\text{miss}}}{E_0} = 1 - \frac{E_{\text{cal}}}{E_0} = \left(N_{\text{ch}}^{\frac{\ln\left(\frac{z}{\ln(-z)}\right)}{\ln^2 N_{\text{ch}}}} \right)^{\ln \frac{2}{3}},$$

where z is defined[3] $z = -\ln N_{\text{ch}} \cdot \frac{m_\pi \cdot c \cdot h_0}{E_0 \cdot \tau \cdot \cos \Theta}$. The most relevant information about the multiplicity considering measurable variables provides the shower maximum $X_{\text{max}} \propto \ln \frac{1}{N_{\text{ch}}}$. Unfortunately, the lack of knowledge of the primary particle

---

[3] m_π and τ are mass and lifetime of charged pion, c is speed of light and h_0 hight in [km].
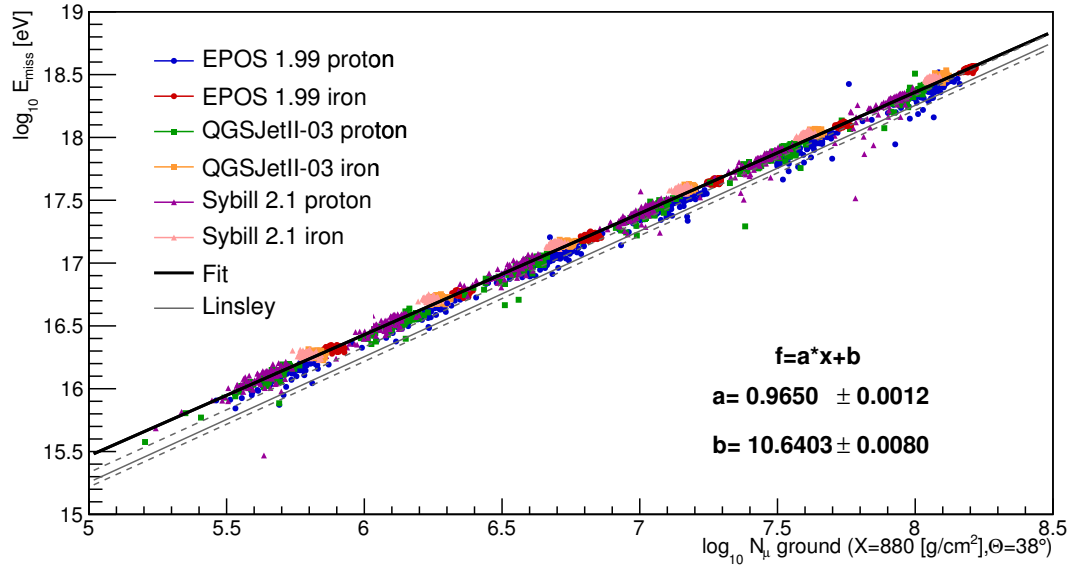
Figure 3.2: Correlation between the number of muons on ground level with energies higher than a 1 GeV and the missing energy, both in logarithmic scale. $36 \cdot 10^3$ showers simulated with CONEX (three different models, proton and iron primaries with $\Theta = 38°$) were used. Besides the linear fit, the result from Linsley [45] also with uncertainties is illustrated.

results in a $\sim 5\%$ difference between protons and iron nuclei. Due to the difference of hadronic models, the systematic uncertainty of the missing energy correction is even higher.

Going back to the origin of the missing energy, muons should attract our attention. Especially, the number of muons at the ground level with energy higher that a 1 GeV is directly correlated with the missing energy. The importance of the amount of muons was already reported by Linsley in [45]. A result depicted in Fig. 3.2 (marked with gray line) was obtained using muon spectra from various experiments. The linear dependence of the invisible energy on the ground muons is shown.

A detailed approach to the determination of the missing energy based on muon correlations has been proposed in [46]. An important observation was demonstrated: the method is independent on primary particle, as well as, on hadronic interaction model. This work was an inspiration for the Fig. 3.2. CONEX with three different interaction models was used for the simulations. As ground level, the value $X_{\text{ground}} = 880/\cos(\Theta)$ [g/cm^2] was taken[4]. Thousand showers were simulated for six energies in the range $10^{17} - 10^{19.5}$ eV, fixed zenith angle $\Theta = 38°$, proton and iron primaries with each model, together $36 \cdot 10^3$ showers. Besides the linear fit, the result from Linsley [45] with uncertainties is included for comparison to simulations.

The exact knowledge of the number of high energy ground muons can eliminate two biggest weaknesses of the standard missing energy determination: dependence on primary particle type and hadronic interaction model. However, this information is not directly obtained with experiments and a new parametrization must be found.

---

[4]The value $X_{\text{ground}} = 880$ [g/cm^2] corresponds to PAO altitude.

3.2 New missing energy parametrization at PAO

A motivation of the new missing energy parametrization was presented in [47]. E_{miss} should not be expressed as a function of E_{cal} because the calorimetric energy is not directly related to the origin of the missing energy. Starting from the Heitler-Matthews model (introduced in Section 1.4), the energy of a primary particle is distributed in an electromagnetic and a hadronic part, N_{em} (N_μ) is number of particles in electromagnetic component (muons) at the shower maximum,

$$E_0 = \xi_c^{\text{em}} N_{\text{em}} + \xi_c^\pi N_\mu,$$

where ξ_c^{em} stands for the critical energy of electromagnetic particles and ξ_c^π for pions. The number of muons is equal (details in Section 1.4) to

$$N_\mu = \beta_0 \left(\frac{E_0}{\xi_c^\pi} \right)^\beta, \tag{3.5}$$

with $\beta = \frac{\ln(N_{\text{ch}})}{\ln\left(\frac{2}{3} N_{\text{ch}}\right)} \sim 0.90 \pm 0.05$. Using this relation, the missing energy can be written as

$$E_{\text{miss}} \propto E_\mu = \xi_c^\pi N_\mu = \xi_c^\pi \beta_0 \left(\frac{E_0}{\xi_c^\pi} \right)^\beta. \tag{3.6}$$

Even if this concept is oversimplified, it is in a good agreement with Matthews prediction of about $\xi_c^\pi \sim 10$ GeV.

The amount of muons is not directly obtained from data at the Pierre Auger Observatory. A measurable quantity with clear relation to the muon number and independence on mass composition is needed. The unique hybrid detector allows to measure S_{1000} and X_{max}. Based on the concept of shower universality, the distance from the shower maximum to the ground $DX = X_{\text{ground}} - X_{\text{max}}$ in [g/cm^2] is used to correct the information from S_{1000}. These two values are available for the new missing energy parametrization. Going back to Eq. 3.6, a power law dependence[5] can be used for the primary energy

$$E_0 = \gamma_0(DX) S_{1000}^\gamma. \tag{3.7}$$

The missing energy as a function of DX and S_{1000} reads

$$E_{\text{miss}} \propto \xi_c^\pi \beta_0 \left(\frac{\gamma_0(DX) S_{1000}^\gamma}{\xi_c^\pi} \right)^\beta,$$

and in a logarithmic form

$$\lg E_{\text{miss}} \propto \overbrace{\lg \xi_c^\pi + \lg \beta_0 + \beta \lg \left(\frac{\gamma_0(DX)}{\xi_c^\pi} \right)}^{A} + \underbrace{\beta\gamma}_{B} \lg S_{1000}. \tag{3.8}$$

---

[5]The usual energy calibration $E_0 = A \cdot S_{1000}^B$ is valid for a fixed zenith angle, but Θ can be replaced in the first order with the fixed stage of shower development DX.

The final function used for the new missing energy parametrization is

$$\lg(E_{\mathrm{miss}}[\mathrm{GeV}]) = A(DX) + B \lg(S_{1000}[\mathrm{VEM}]). \tag{3.9}$$

Once the constants A and B are known from simulations[6], the missing energy can be calculated event-by-event for Golden hybrids, see Fig. 3.3. These values are used for the fit to obtain a new missing energy model as a function of E_{cal}, which is utilized for all hybrid events. The results are shown at the Fig. 3.4 together with a comparison to the standard Barbosa results from a different interaction models.

_____

[6]Parameter A needs to be corrected, as described in the next chapter, in oder to be independent on primary particles type as well as on interaction model ([36] and [48]).
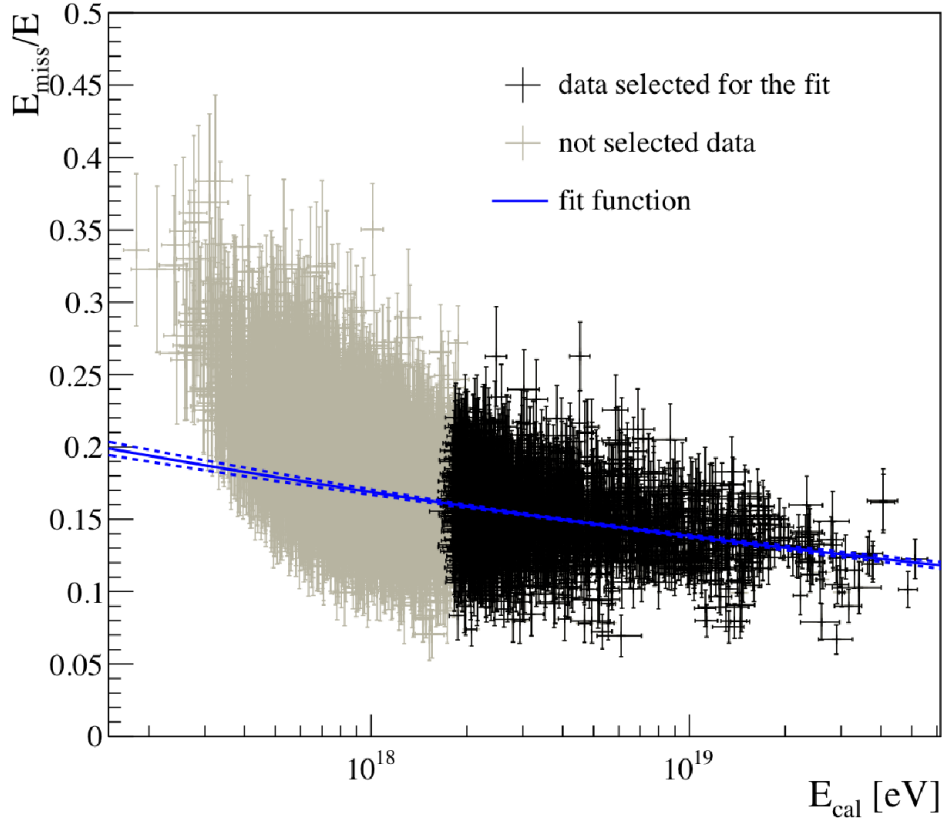
Figure 3.3: Dependence of the fraction of the missing energy on E_{cal} measured from hybrid events, where the energy of the primary particle was calculated with the new parametrisation of the missing energy $E = E_{\mathrm{cal}} + E_{\mathrm{miss}}(DX, S_{1000})$. Dashed lines around the fit represent statistical errors. Taken from [36].
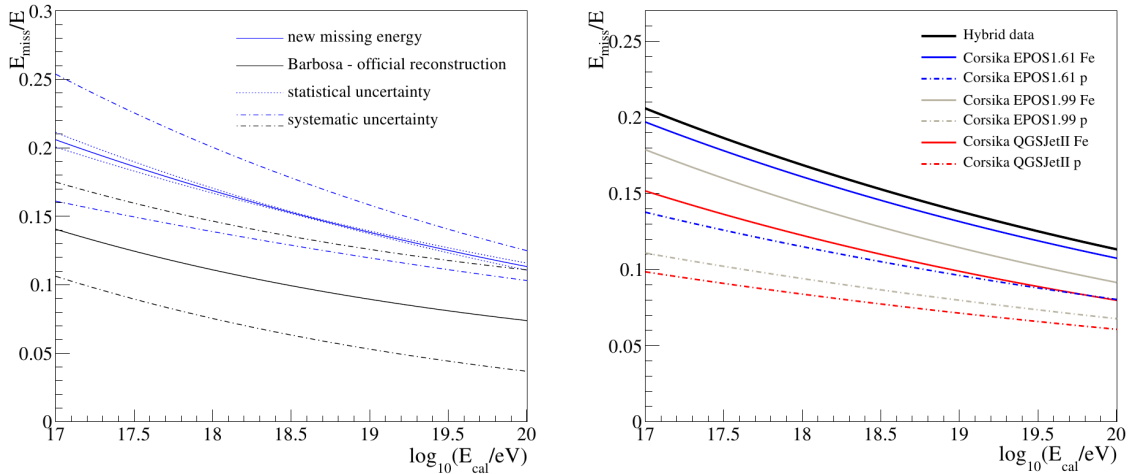

Figure 3.4: Comparison of the new model of the missing energy $E_{\mathrm{miss}}(DX, S_{1000})$ to the official Barbosa reconstruction (on the left side) and to the different hadronic model prediction (on the right). Taken from [36].

Chapter 4

The missing energy for Infill Array

What are the differences between regular and Infill array at the Pierre Auger Observatory considering estimation of the missing energy? In this chapter, we search for an answer to this question.

Cosmic ray air showers caused by a particle with lower energy need less cascade steps n (referring to Heitler-Matthews model described in Sec. 1.4) to reach the shower maximum. Hence fewer electromagnetic subshowers which are measured as a calorimetric energy with fluorescence detector arise in the air shower. This means that low energy showers contain naturally larger invisible energy fraction, see for example Fig. 3.1. An exact estimation of the missing energy at lower energies is thus a very important task.

One of the motivations for this work is clearly illustrated on Fig. 3.3. The missing energy was calculated for selected data with the new function 3.9. The result was fitted in order to obtain the new missing energy also as a function of the calorimetric energy. Just the data with $E_{\mathrm{cal}} > 10^{18.3}$ eV were used for the fit. Events denoted with gray color (unselected) show a clearly steeper character. This can be a consequence of the surface detector trigger efficiency. The water tanks from the regular surface array are not fully efficient at energies under 10^{18} eV and they are triggering mostly the events with more muons and consequently with the higher missing energy. These data were left out from the fit. For the air showers with lower energy just an extrapolation is used.

At the Pierre Auger Observatory, we are able to detect cosmic ray air showers down to 10^{17} eV with the new Infill array extension (described in section 2.2). In the energy range up to $10^{18.3}$ eV, data from the Infill array can be selected. There is no need to face up the problem with trigger efficiency at energies around 10^{18} eV, mentioned above. A new fitted function will be obtained for lower energies which replace the extrapolated part of the $E_{\mathrm{miss}}(E_{\mathrm{cal}})$. For this purpose, the function 3.9 is substituted with

$$\lg(E_{\mathrm{miss}}[\mathrm{GeV}]) = A^{\mathrm{Infill}}(DX) + B^{\mathrm{Infill}} \lg(S_{450}[\mathrm{VEM}]), \qquad (4.1)$$

where A^{Infill} and B^{Infill} differ from the parameters in Eq. 3.9. The value S_{450} [VEM] for the Infill array (spacing 750 m) is analogical to S_{1000} [VEM] for the regular array.
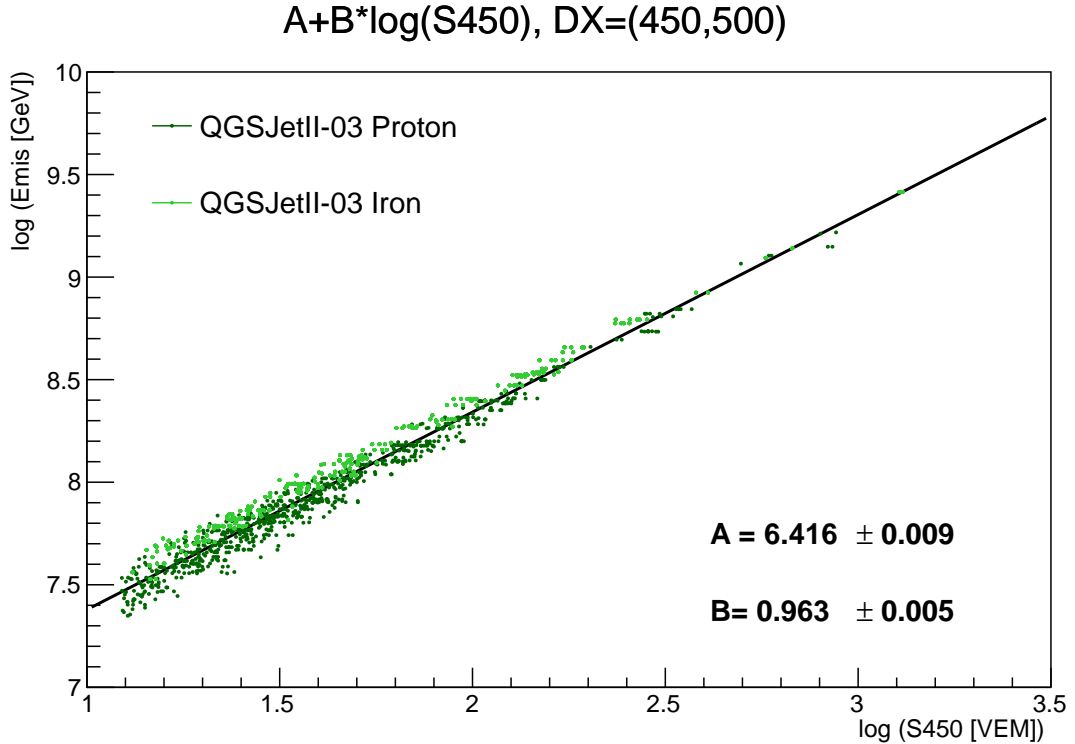
Figure 4.1: Dependence of the SD detector signal S_{450} [VEM] on the missing energy for $DX = 450 - 500$ [g/cm^2]. E_{mis} [GeV] was computed as a difference between the energy of primary particle and the calorimetric energy, both taken from Monte Carlo informations about generated shower.

4.1 Estimation of the parameters A^{Infill} and B^{Infill}

In the following text, A^{Infill} and B^{Infill} will be labeled just A and B, for simplification. In order to obtain the new missing energy parametrisation, we need to evaluate these two values. The derivation of the both parameters in the previous chapter implies that B equals a constant and A is a function of DX. The concept of shower universality says that after a shower reaches its maximum, further development is universal for proton and iron showers. An information about an amount of atmosphere depth [g/cm^2] the shower cascade crossed is hidden in the distance of the shower maximum to ground $DX = X_{\mathrm{ground}} - X_{\mathrm{max}} = 880/\cos(\Theta) - X_{\mathrm{max}}$. Thus for fixed DX, we expect Eq. 4.1 to be a linear function. For verification of this assumption, a range $DX = 200 - 850$ [g/cm^2] was divided in 13 bins and in each one a fit with linear function was performed (for fixed $DX : A(DX) \to A$). An example of one bin ($DX = 450 - 500$) is illustrated on Fig. 4.1. The fits in all DX bins are added to Appendix. Results obtained for A and B in individual bins are depicted on Fig. 4.2 resp. Fig. 4.3 (dark blue).
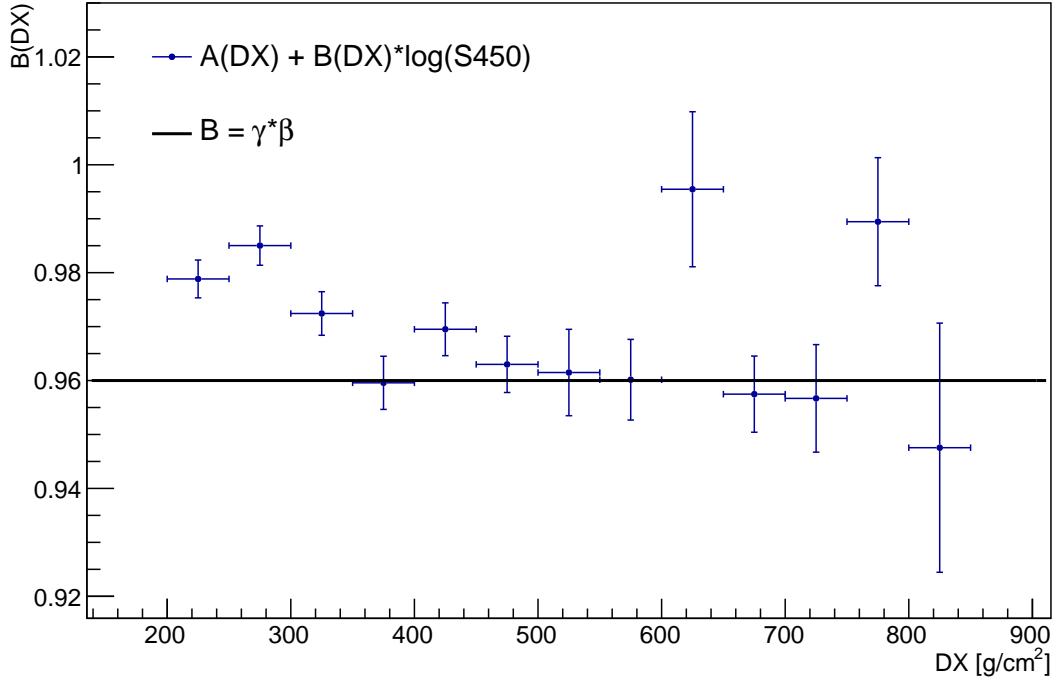
Figure 4.2: Estimation of the parameter B. Dark blue markers represent values obtained from the linear fit (Fig. 4.1) in every DX bin. This method is compared with $B = \beta\gamma = 0.96$ (black line).

Investigation of the parameter B is illustrated on Fig. 4.2. Dark blue markers represents values of B from linear fit of Eq. 4.1 in different DX bins. Parameter B is a multiple of two other constants, as follows from Eq. 3.8, concrete of β from Eq. 3.5 and γ from Eq. 3.7. Parameter γ is different for Infill array and Eq. 3.7 changes to $E = \gamma_0(DX)S_{450}^\gamma$. As was presented in [32], the value of the parameter from simulations with model QGSJetII-03 for mixed composition is $\gamma = 1.0095$. Parameter β depends first of all on pion multiplicity, but also on inelasticity of the first interaction and division of the energy to charged and neutral pions. Based on the study in [25] and [49], we used the value of the parameter $\beta = 0.95$. This gives the value $B = \beta\gamma = 0.96$ (black line) which is comparable to the fitted values B shown in Fig. 4.2. For this reason we have decided to use B(=0.96) constant and independent on DX for the final missing energy parametrisation.

Estimation of $A(DX)$ is represented on Fig. 4.3. Similarly as for B, dark blue markers are dedicated to values from linear fit of Eq. 4.1 in every DX bin. The parameter $A(DX)$, as introduced in Eq. 3.8, has a form

$$A(DX) = \lg \xi_c^\pi + \lg \beta_0 + \beta \lg \left(\frac{\gamma_0(DX)}{\xi_c^\pi} \right). \qquad (4.2)$$

Parameters $\beta_0, \gamma_0, \xi_c^\pi$ are obtained from fits of Eq. 3.5 and Eq. 3.7 for individual DX bins (γ and β were taken as constants with the same values as for estimation of B). Resulting $A(DX)$ calculated from Eq. 4.2 is plotted in light blue color. It is evident that $A(DX)$ values obtained by this approach do not correspond exactly to
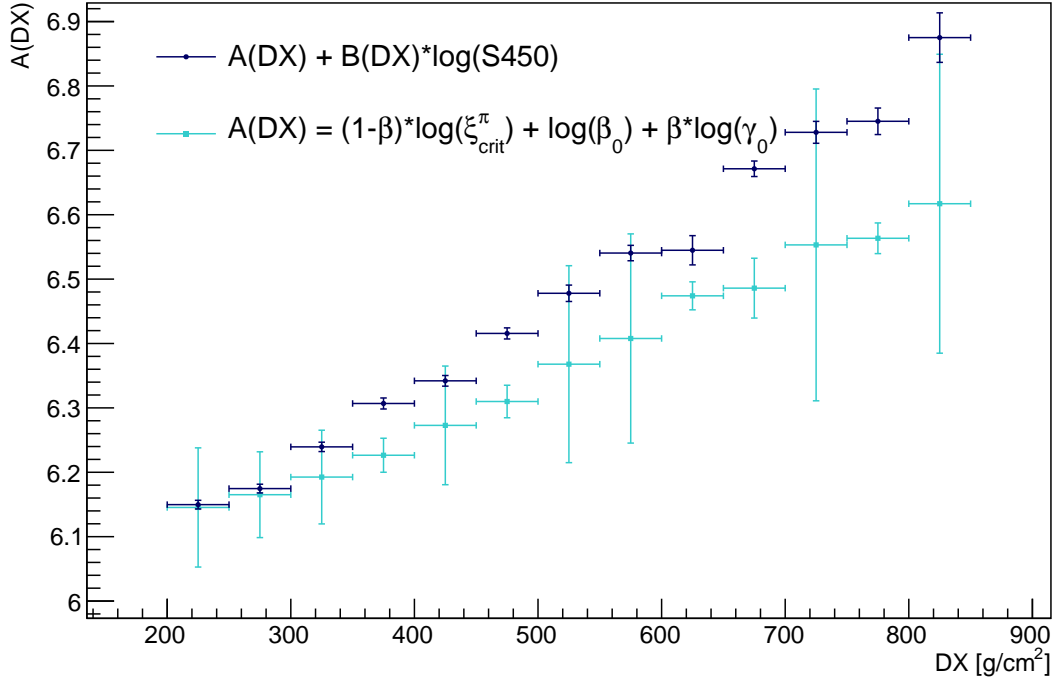
Figure 4.3: Estimation of the parameter A. Dark blue markers represent values obtained from the linear fit (Fig. 4.1) in every DX bin. This method is compared with definitions of both parameters, where the values of $\gamma(\gamma_0)$ and $\beta(\beta_0)$ were fitted in individual DX bins.

$A(DX)$ from Eq. 4.1 in every DX bin. We suspect that the origin of the difference arises from our fit of Eq. 3.5. Values of β_0 and ξ_c^π suffer from an assumption that number of muons on ground shows the same behavior as the number of muons in shower maximum (N_μ in Eq. 3.5 denotes number of muons in shower maximum). Detailed understanding of remaining differences in Fig. 4.3 will be subject of further study and it is outside of scope of this thesis. It is important, that although both approaches have different basis, they show consistently growing trend of A with increasing DX.

Once the parameter B is fixed, there is a more straight forward method for the calculation of $A(DX)$,

$$A(DX) = \lg(E_{\mathrm{miss}}[\mathrm{GeV}]) - B\lg(S_{450}[\mathrm{VEM}]). \tag{4.3}$$

We used this equation to parametrise the function $A(DX)$, as shown on Fig. 4.4. Set of events simulated with interaction model QGSJetII-03 (details about simulation, reconstruction and applied cuts are in Appendix) consists of more than $17 \cdot 10^3$ proton and iron showers. A discussion about a limitation of the DX range can be found in Appendix. We choose a second degree polynomial as a fitting function for mixed composition:

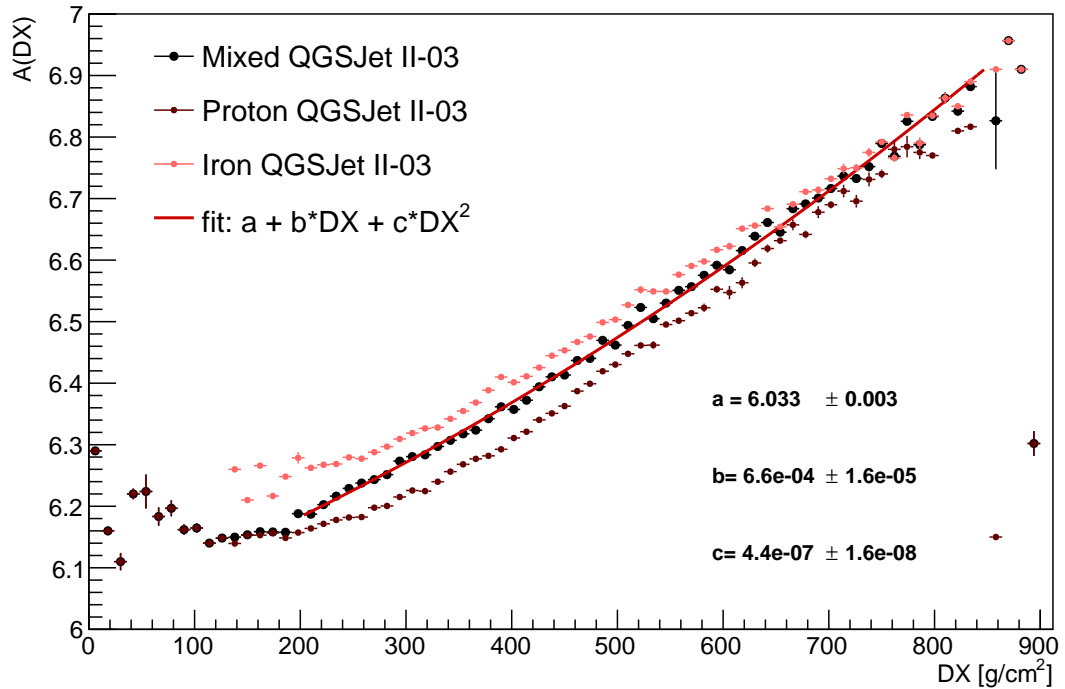$$A(DX) = a + b \cdot DX + c \cdot DX^2. \tag{4.4}$$

33

Figure 4.4: Profile of the function $A(DX)$ computed from Eq. 4.3 from all simulated events (black dots) compared with the profile from proton and iron showers (dark resp. light red). The resulting fit was done in the range $DX = 200 - 850$ [g/cm^2] for mixed composition, plotted with red line.

Individual parameters of this equation were estimated from the fit:

$$a = 6.033 \pm 0.003$$
$$b = 6.64 \cdot 10^{-4} \pm 1.6 \cdot 10^{-5}$$
$$c = 4.4 \cdot 10^{-7} \pm 1.6 \cdot 10^{-8}$$

Finally, we have fully defined the new missing energy function 4.1 for Infill array. The comparision to the standard estimation of the missing energy (Barbosa method) is demonstrated on Fig. 4.5.

4.2   Correction factor for $A(DX)$

For Golden hybrids, X_{max} and S_{450} are available and the missing energy can be directly obtained from the new function 4.1. Parameters $A(DX)$ and B were acquired from the fit of simulations. As we see on Fig. 4.5, our new method of determination of the missing energy is more precise than the official Barbosa method, but it shows still some remaining dependence on primary particle type. We believe that the missing energy is strongly related to muon content (in our parametrisation to $X_{\mathrm{max}}, \cos(\Theta)$ and S_{450}) and for arbitrary energy it should not depend on mass composition. For this reason, we need to add an correction term to Eq. 3.5. Hadronic

34

models in Monte Carlo simulations have certain limitations and they differ from each other. The biggest weakness is the description of the muon number and attenuation curve [50]. It means that values γ_0 and β_0 need to be corrected

$$\lg E_{\text{mis}}^{\text{mc}} = \lg E_{\text{mis}}^{\text{QJ3}} + \lg \frac{E_{\text{mis}}^{\text{mc}}}{E_{\text{mis}}^{\text{QJ3}}} =$$

$$A^{\text{QJ3}}(DX) + B^{\text{QJ3}} \cdot S_{450} + \underbrace{A^{\text{mc}}(DX) - A^{\text{QJ3}}(DX)}_{\Delta A} + \underbrace{(B^{\text{QJ3}} - B^{\text{mc}})}_{\Delta B} \cdot S_{450}.$$

Our referring Monte Carlo model QGSJetII-03 (mixed composition) is labeled with QJ3 index. Instead of mc, different models with one type of primary particle will be used.

If we recall the definition of $A(DX)$ (4.2) and $B = \gamma\beta$, the correction factors are hidden in ΔA and ΔB:

$$\Delta B = (\beta^{\text{QJ3}} + \Delta\beta)(\gamma^{\text{QJ3}} + \Delta\gamma) - \beta^{\text{QJ3}}\gamma^{\text{QJ3}} = \Delta\beta\Delta\gamma + \Delta\beta\gamma^{\text{QJ3}} + \Delta\gamma\beta^{\text{QJ3}}$$

$$\Delta A = \Delta\beta \lg \xi_c^\pi + \lg \frac{\beta_0^{\text{mc}}}{\beta_0^{\text{QJ3}}} + \lg \frac{(\gamma_0^{\text{mc}})^{\beta^{\text{mc}}}}{(\gamma_0^{\text{QJ3}})^{\beta^{\text{QJ3}}}} = \Delta\beta \lg \xi_c^\pi + \lg \left[\frac{(\gamma_0^{\text{mc}})^{\beta^{\text{mc}}}}{(\gamma_0^{\text{QJ3}})^{\beta^{\text{QJ3}}}} \cdot \frac{\beta_0^{\text{mc}}}{\beta_0^{\text{QJ3}}} \right].$$

Under the assumption that the uncertainties in Monte Carlo arise only in β_0 and γ_0, the correction term reduces just to the second part of $\Delta A(DX)$. The missing energy function we want to use has a form of [48]:

$$\lg E_{\text{mis}}^{\text{mc}} = \lg E_{\text{mis}}^{\text{QJ3}} + \lg \left[\left(\frac{\gamma_0^{\text{mc}}}{\gamma_0^{\text{QJ3}}} \right)^\beta \frac{\beta_0^{\text{mc}}}{\beta_0^{\text{QJ3}}} \right]. \tag{4.5}$$

The correction of the attenuation curve $\gamma_0(DX)$ is a fit parameter from energy dependence on S_{450} in different DX bins. Similarly, β_0 is obtained from the fit of Eq. 3.5. We suspect that the inconsistency of N_μ in shower maximum and on ground is not present here because only the parameter ratio $(\frac{\beta_0^{\text{mc}}}{\beta_0^{\text{QJ3}}})$ is relevant.

In the first step, we evaluate the correction factor for simulation set QGSJetII-03 separately for proton and iron showers (our referring set consists of 50% protons and 50% iron showers). Indeed, Fig. 4.5 loses after correction from Eq. 4.5 the primary particle dependence, see Fig. 4.6.

In the next steps, we compute the correction factors for new (from 2013) Monte Carlo models: EPOS LHC and QGSJetII-04. In two figures (for lucidity), we compare the standard Barbosa method (Fig. 4.7) to our new parametrisation (Fig. 4.8).
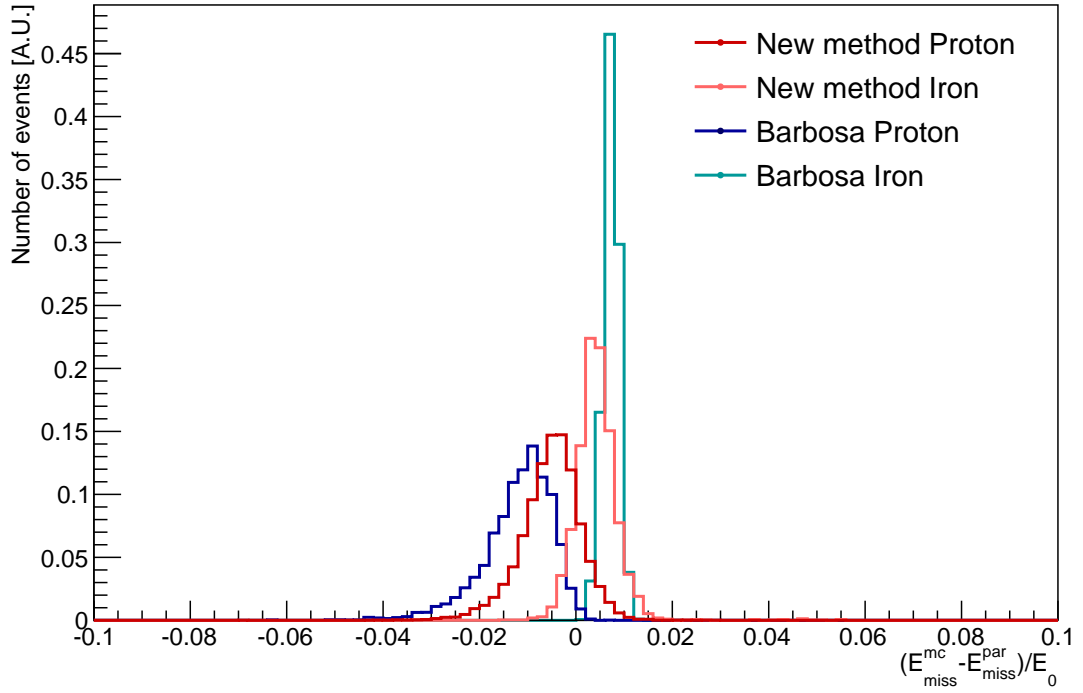
Figure 4.5: Residuals of $(E_{\mathrm{mis}}^{\mathrm{mc}} - E_{\mathrm{mis}}^{\mathrm{par}})/E_0$. An official missing energy parametrisation (Barbosa) is compared to the new missing energy parametrisation, where $E_{\mathrm{mis}}^{\mathrm{par}}$ is computed from Eq. 4.1. Histograms are normalized to 1.

Figure 4.6: Residuals of $(E_{\mathrm{mis}}^{\mathrm{mc}} - E_{\mathrm{mis}}^{\mathrm{par}})/E_0$. An official missing energy parametrisation (Barbosa) is compared to the new missing energy parametrisation, where $E_{\mathrm{mis}}^{\mathrm{par}}$ is computed from Eq. 4.1 and corrected with Eq. 4.5. Histograms are normalized to 1.
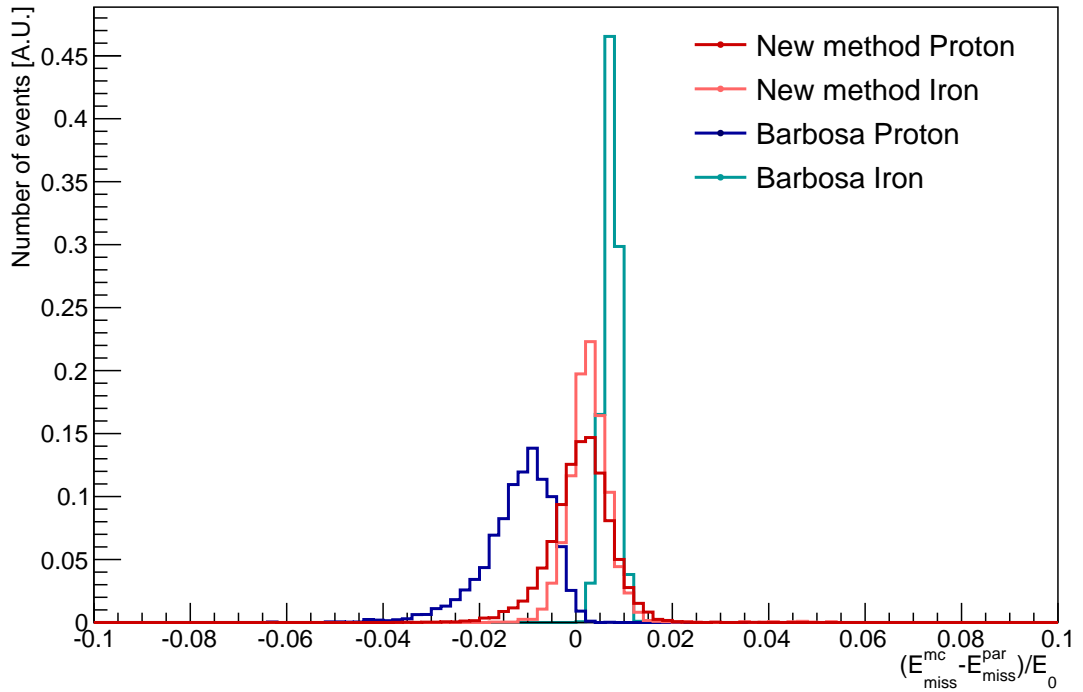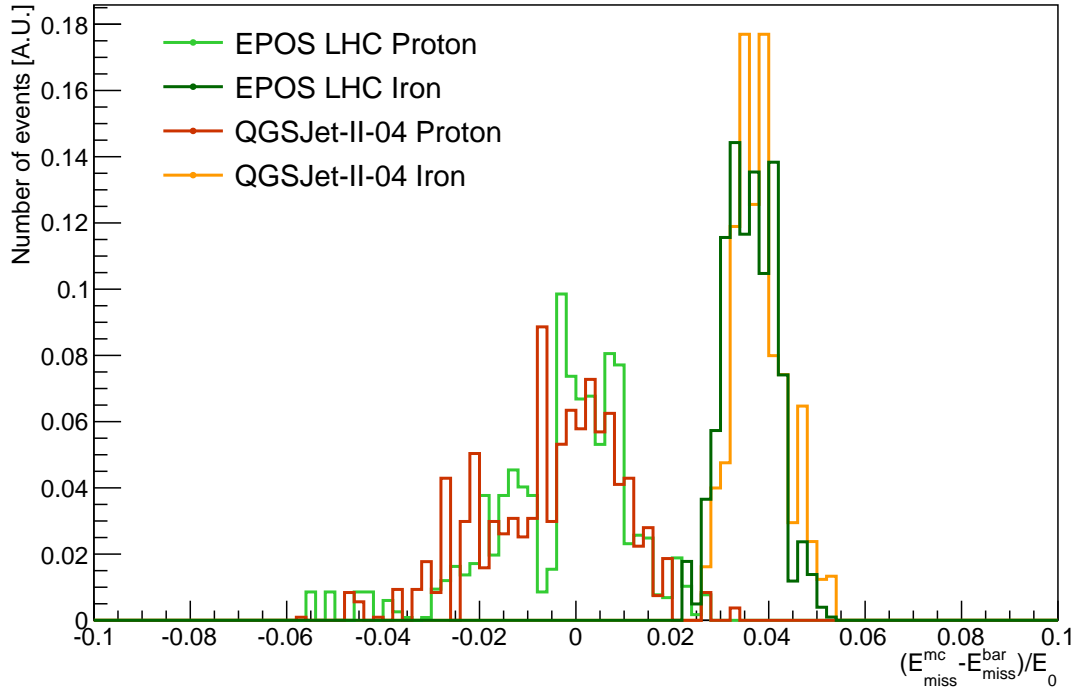
Figure 4.7: Residuals of $(E_{\text{mis}}^{\text{mc}} - E_{\text{mis}}^{\text{bar}})/E_0$. An official missing energy parametrisation (Barbosa) is used for evaluation of the missing energy for two Monte Carlo models and two primary particles. Histograms are normalized to 1.
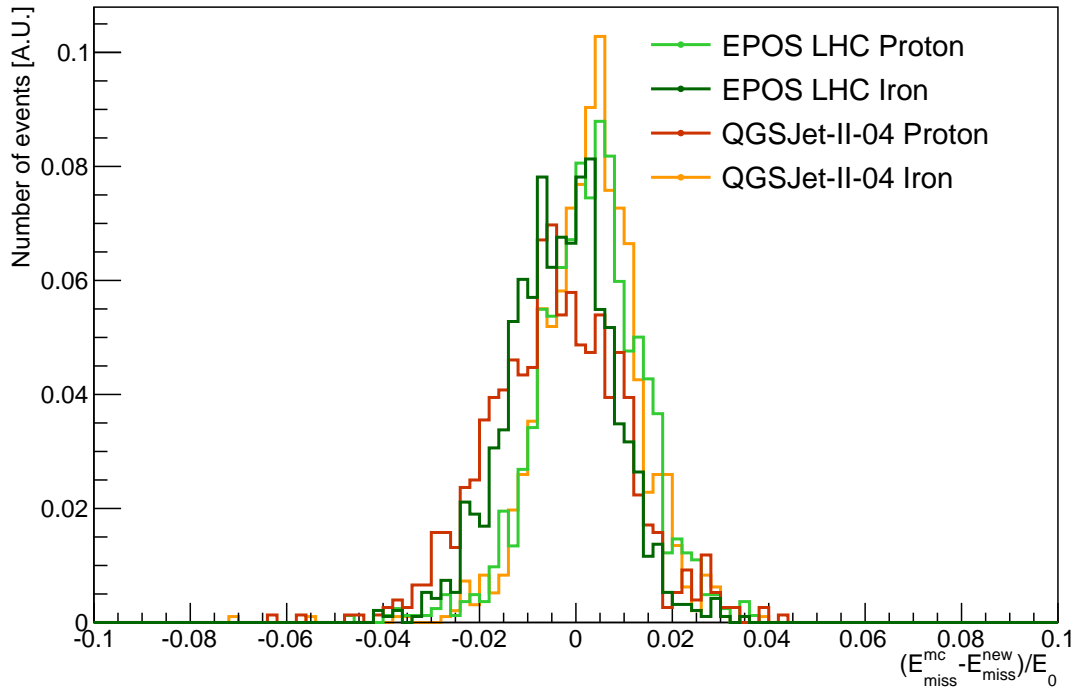

Figure 4.8: Residuals of $(E_{\text{mis}}^{\text{mc}} - E_{\text{mis}}^{\text{new}})/E_0$. The new missing energy parametrisation, where $E_{\text{mis}}^{\text{new}}$ is computed from Eq. 4.1 and corrected with Eq. 4.5, is shown for two different Monte Carlo models and two primary particles. Histograms are normalized to 1.

4.3 Parametrisation of the missing energy from data

Before we use the new parametrisation for the real data, we have to modify the correction factor.

$$\lg E_{\text{mis}}^{\text{data}} = \lg E_{\text{mis}}^{\text{QJ3}} + \lg \frac{E_{\text{mis}}^{\text{data}}}{E_{\text{mis}}^{\text{QJ3}}}$$

$$\lg E_{\text{mis}}^{\text{data}} = \lg E_{\text{mis}}^{\text{QJ3}} + \lg \left[\left(\frac{\gamma_0^{\text{data}}}{\gamma_0^{\text{QJ3}}} \right)^{\beta} \frac{\beta_0^{\text{data}}}{\beta_0^{\text{QJ3}}} \right]. \tag{4.6}$$

The correction of the attenuation curve $\gamma_0^{\text{data}}(DX)$ is a fit parameter from energy dependence on S_{450} in different DX bins. The corresponding γ_0^{QJ3} is obtained analogically just with simulated events instead of the measured data (plots available in Appendix). Number of muons can not be corrected in the same way. There is no (not working now) possibility to measure muons directly. We believe that in very inclined showers, the electromagnetic component is already absorbed and we measure pure muon signal. From analysis based on this principle we can get the factor $\frac{\beta_0^{\text{data}}}{\beta_0^{\text{mc}}}$. The parameter N_{19} was evaluated only for regular array, but the ratio of the amount of muons from data and Monte Carlo has constant character with energy ([51]) and hence we just extrapolate it to the lower energies. We take for this factor the same value as in Mariazzi work [48], $\frac{\beta_0^{\text{data}}}{beta_0^{\text{mc}}} = 1.97 \pm 0.10\,\text{sys} \pm 0.04\,\text{stat}$. We estimated the correction factor for 8 bins in the range $DX = 200 - 600$ because there is not enough measured data available out of this interval, see Fig. 4.9. The correction was fitted with third degree polynomial and the complete function $A(DX)$ for data is expressed as

$$A^{\text{data}}(DX) = A^{\text{QJ3}}(DX) + \underbrace{a_1 + b_1 DX + c_1 DX^2 + d_1 DX^3}_{\text{Correction}} \tag{4.7}$$

with obtained parameter values

$$a_1 = -0.018$$
$$b_1 = 1.4 \cdot 10^{-3}$$
$$c_1 = -3.3 \cdot 10^{-6}$$
$$d_1 = 2.1 \cdot 10^{-9}$$

At this point, we can use the new missing energy function with the correction term for Golden Hybrid data from HeCo (details about data set in Appendix). On Fig. 4.10 it is applied the new missing energy to measured data. Selected events must fulfill Trigger Efficiency condition (untriggered marked with gray color). The resulting fit (magenta color) is compared to the extrapolated fit from regular array (black color), presented in [52]. We estimated the new missing energy as a function of the calorimetric energy and we can use the parametrisation for all data, where E_{cal} is measured (not just golden hybrids).

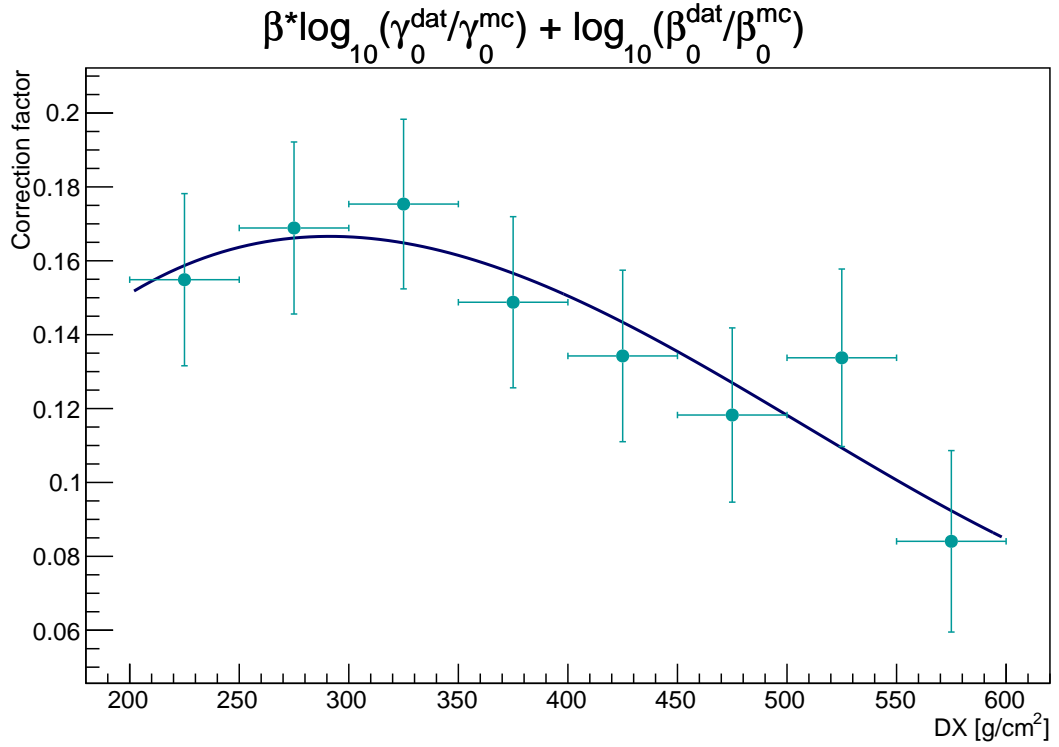$$\beta*\log_{10}(\gamma_0^{dat}/\gamma_0^{mc}) + \log_{10}(\beta_0^{dat}/\beta_0^{mc})$$

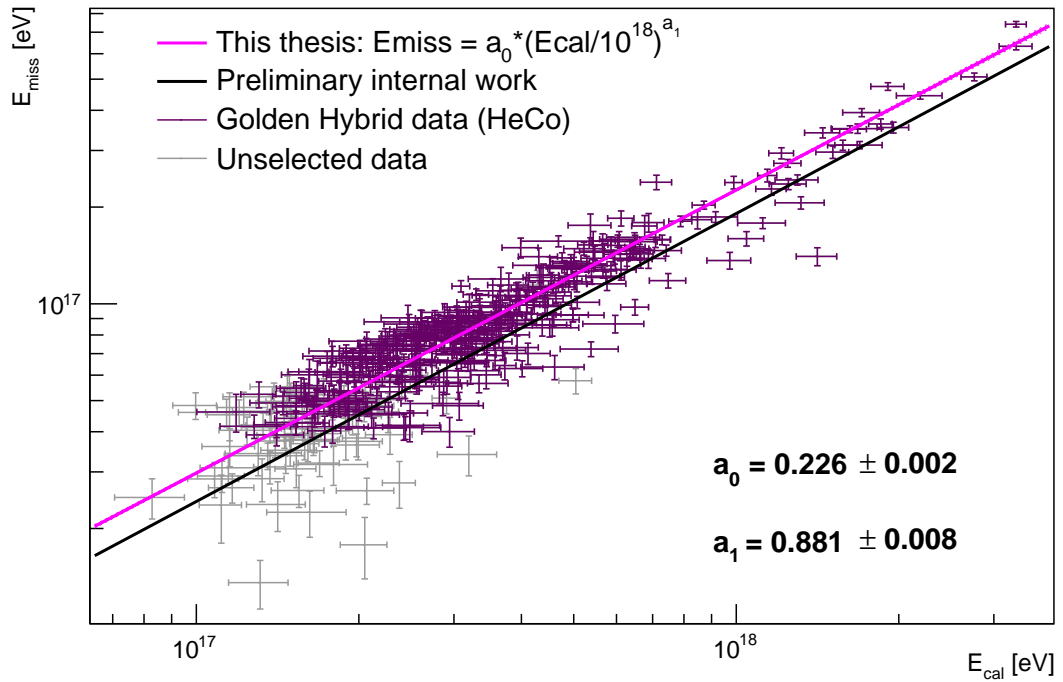Figure 4.9: Fit of the correction factor from the Eq. 4.6 for eight bins in $DX = 200 - 600$.

Figure 4.10: New missing energy $E_{mis}(DX, S_{450})$ computed for Golden Hybrid events (HeCo+Infill) from Eq. 4.1 with correction from Eq. 4.6 plotted as a function of calorimetric energy E_{cal}. The resulting fit to the selected events (fulfilling the Trigger Efficiency condition, marked with violet color) is compared to the extrapolated fit from regular array presented in [52].

4.4 Effect of the shift in the energy scale

In order to see the difference in energy shift between individual methods of the missing energy estimation, E_{mis} was plotted as a fraction of E_{cal} on Fig. 4.11.

Gray line shows the Barbosa prediction and the gray dashed line is a band of 4% in y-axis for Barbosa method. This 4% is the value of systematic uncertainty at energies 10^{18} eV. The systematic errors are smaller for higher energies and they increase in lower energy range. Therefore the gray dashed line has just illustrative character and we can not take it as absolute systematic uncertainty.

The black line on the same figure represents the preliminary results from [52]. Systematic uncertainties for this method were determined in [48] to be 2%. This value is not valid for extrapolated part of the curve and therefore the black dashed line has also just illustrative character, representing 2%.

For the result of this thesis (magenta line on Fig. 4.11) systematic errors were preliminary estimated (based on the Fig. 4.8) to 2% as well. Similarly, the magenta dashed lines show 2% bands.

Barbosa parametrisation is the official way how the missing energy is taken into account in standard data reconstruction at Pierre Auger Observatory. Underestimation of the missing energy by Barbosa method is evident. This method is based only on Monte Carlo simulations, which does not describe amount of muons precisely (predicts less muons). This very probably implies also the small missing energy fraction.

The new missing energy parametrisation (Mariazzi [48]) is trying to fix this problem and the estimation is based on measured values, closely related to the origin of the missing energy. The resulting fit for $E_{\mathrm{mis}}(E_{\mathrm{cal}})$ was obtained from the data from the regular array, for events with energy above $10^{18.3}$ eV. The missing energy for showers caused by a primary particle with lower energy is computed from the extrapolation of this fit.

The aim of this thesis was to prove on data from Infill array if such extrapolation is sufficient. The fraction of the missing energy differs by 4% at energies 10^{18} eV and rises to almost 6% by $E = 10^{17}$ eV. As a conclusion we do not suggest to use the extrapolated $E_{\mathrm{mis}}(E_{\mathrm{cal}})$ function. We recommend a further investigation with combined data set from regular as well as Infill array and perform the fit in full range $10^{17} - 10^{20}$ eV.
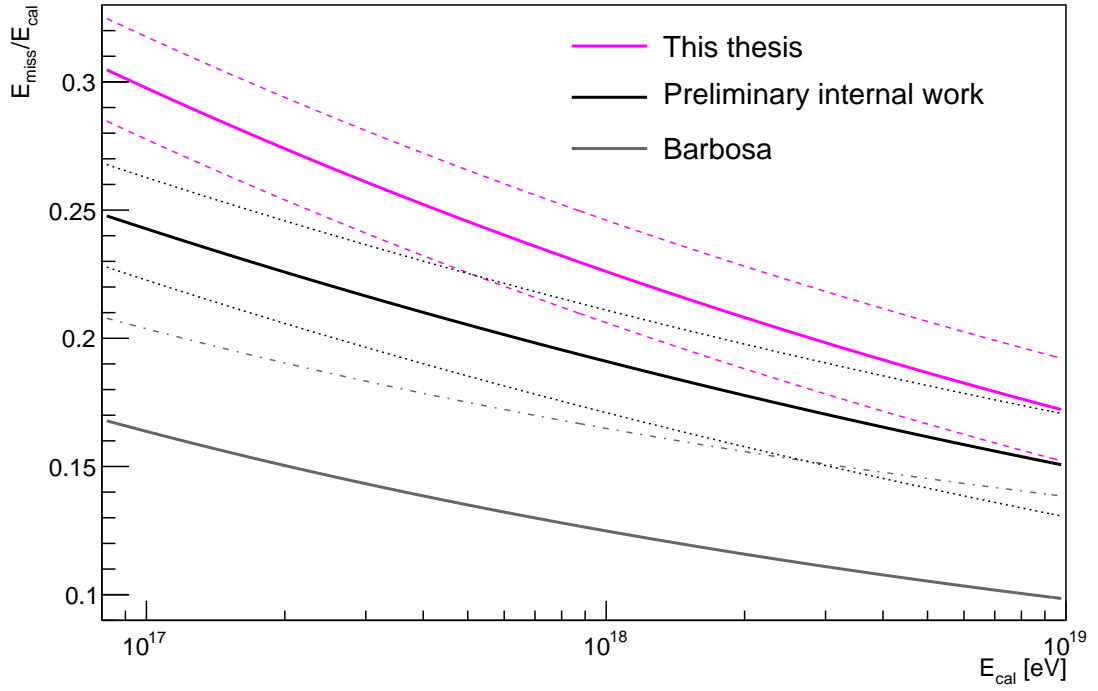
Figure 4.11: Fraction of the missing energy as a function of E_{cal}. The official method (Barbosa from [42]) is compared with the new method of estimation of the missing energy (presented in [52]) for regular array and to the resulting fit presented in this thesis. The dashed lines show an approximation of the systematic uncertainty of the methods.

Conclusion

After the introduction into the field of astroparticle physics in the first chapter, the biggest experiment in this area, Pierre Auger Observatory was introduced in the following part of the thesis.

The third chapter was focused on the missing energy, where the importance and difficulties of its estimation were explained. On the example of Pierre Auger Observatory, improvements in the method of calculation of the missing energy was discussed. An foreword for the main part of this thesis was presented.

The aim of this master thesis was to investigate recently proposed method to calculate missing energy in cosmic ray showers for data from the Pierre Auger Observatory. The method was newly applied on data from the Infill array, which typically measures showers at energies a decade lower than the main array. At these low energies, the missing energy correction plays even more important role. All the key steps of the method developed in [48] for the main array were repeated in this thesis for the Infill array. Finally, estimation of the missing energy on real data was presented. The results reported in this thesis shall be considered as preliminary and will be subject of further analysis and crosschecks. They show, however, that the missing energy at low energies ($\sim 10^{17}$ eV) can be much higher than what is proposed by the official and currently used reconstruction method (Barbosa parametrisation).

Bibliography

[1] D. dEnterria, R. Engel, T. Pierog, S. Ostapchenko, and K. Werner. Constraints from the first lhc data on hadronic event generators for ultra-high energy cosmic-ray physics. *Astroparticle Physics*, 35(2):98–113, 2011.

[2] D. R. Bergman and J. W. Belz. Cosmic rays: the second knee and beyond. *Journal of Physics G: Nuclear and Particle Physics*, 34(10):R359, 2007.

[3] T. Stanev. *High energy cosmic rays*. Springer, 2010.

[4] A. M. Hillas. Cosmic rays: Recent progress and some current questions. *arXiv preprint astro-ph/0607109*, 2006.

[5] E. Fermi. On the origin of the cosmic radiation. *Physical Review*, 75(8):1169, 1949.

[6] A.M. Hillas. The origin of ultra-high-energy cosmic rays. *Annual Review of Astronomy and Astrophysics*, 22:425–444, 1984.

[7] K. Fang, K. Kotera, and A. V. Olinto. Ultrahigh energy cosmic ray nuclei from extragalactic pulsars and the effect of their galactic counterparts. *Journal of Cosmology and Astroparticle Physics*, 2013(03):010, 2013.

[8] K. Greisen. End to the cosmic-ray spectrum? *Physical Review Letters*, 16(17):748–750, 1966.

[9] G. T. Zatsepin and V. A. Kuz'Min. Upper limit of the spectrum of cosmic rays. *JETP Lett.(USSR)(Engl. Transl.)*, 4, 1966.

[10] J.W. Cronin. Cosmic rays: the most energetic particles in the universe. *Reviews of Modern Physics*, 71(2):165–172, 1999.

[11] R. Aloisio. Ultra high energy cosmic rays propagation and spectrum. *arXiv preprint arXiv:1104.0329*, 2011.

[12] D. Hooper and A. M. Taylor. On the heavy chemical composition of the ultra-high energy cosmic rays. *Astroparticle Physics*, 33(3):151–159, 2010.

[13] T. Wulf. On the radiation of high penetrating power that exists in the atmosphere. *Phys. Zeit*, 1:152–157, 1909.

[14] J. Grygar and R. Šmída. Door meten tot weten. *Československý časopis pro fyziku*, 58(2):116, 2008.

[15] P. Auger, P. Ehrenfest, R. Maze, J. Daudin, and R. A. Fréon. Extensive cosmic-ray showers. *Reviews of Modern Physics*, 11(3-4):288–291, 1939.

[16] K. H. Kampert and A. A. Watson. Extensive air showers and ultra high-energy cosmic rays: a historical review. *The European Physical Journal H*, pages 1–54, 2012.

[17] R. Engel, D. Heck, and T. Pierog. Extensive air showers and hadronic interactions at high energy. *Annual Review of Nuclear and Particle Science*, 61:467–489, 2011.

[18] D Heck, J. Knapp, J. N. Capdevielle, G. Schatz, T. Thouw, et al. *CORSIKA: A Monte Carlo code to simulate extensive air showers*, volume 6019. FZKA, 1998.

[19] D. Heck and T. Pierog. Corsika users guide. *http://www-ik.fzk.de/ corsika/*.

[20] K. Werner and T. Pierog. Current concepts in theory and modelling of high energy hadronic interactions. *Moving Forward into the LHC Era*, 17:279, 2010.

[21] S. Ostapchenko. High energy cosmic ray interactions-an overview. In *Journal of Physics: Conference Series*, volume 60, page 167. IOP Publishing, 2007.

[22] T. Bergmann et al. One-dimensional hybrid approach to extensive air shower simulation. *Astropart. Phys.*, 26:420–432, 2007.

[23] T. Pierog et al. First results of fast one-dimensional hybrid simulation of eas using conex. *Nucl. Phys. Proc. Suppl.*, 151:159–162, 2006.

[24] G. Bossard et al. Cosmic ray air shower characteristics in the framework of the parton-based gribov-regge model nexus. *Phys. Rev.*, D63:054030, 2001.

[25] J. Matthews. A heitler model of extensive air showers. *Astroparticle Physics*, 22(5):387–397, 2005.

[26] M. Maur. Improving the composition sensitivity of the pierre auger observatory with additional scintillators. *Internal Auger Note,GAP-2012-151*, 2012.

[27] S. Argiro, S. L. C. Barroso, J. Gonzalez, L. Nellen, T. Paul, T. A. Porter, L. Prado Jr, M. Roth, R. Ulrich, and D. Veberič. The offline software framework of the pierre auger observatory. *Nuclear Instruments and Methods in Physics Research Section A: Accelerators, Spectrometers, Detectors and Associated Equipment*, 580(3):1485–1496, 2007.

[28] J. Abraham, P. Abreu, M. Aglietta, C. Aguirre, E. J. Ahn, D. Allard, I. Allekotte, J. Allen, P. Allison, J. Alvarez-Muñiz, et al. The fluorescence detector of the pierre auger observatory. *Nuclear Instruments and Methods in Physics Research Section A: Accelerators, Spectrometers, Detectors and Associated Equipment*, 620(2):227–251, 2010.

[29] Auger Collaboration. The pierre auger project design report. *Fermi International Accelerator Laboratory*, 1997.

[30] R. Šmída. Cosmic-ray physics with the pierre auger observatory. *Charles University, PhD. thesis, available at: http://www-hep2.fzu.cz/ smida/www/dizertace-smida.pdf*, 2009.

[31] F. Sanchez. The amiga detector of the pierre auger observatory: an overview. *Proc. of the 32nd ICRC, Beijing, China*, 2011.

[32] A. Schulz. Measurement of the energy spectrum of cosmic rays between 0.1 eev and 30 eev with the infill extension of the surface detector of the pierre auger observatory. *Internal Auger Note,GAP-2012-136*, 2012.

[33] T. H. J. Mathes and Collaboration Pierre Auger. The heat telescopes of the pierre auger observatory status and first data. *Proc. of the 32nd ICRC, Beijing, China*, 2011.

[34] P. Abreu, M. Aglietta, E. J. Ahn, I. F. M. Albuquerque, D. Allard, I. Allekotte, J. Allen, P. Allison, J. Castillo, J. Alvarez-Muñiz, et al. The pierre auger observatory iv: Operation and monitoring. *arXiv preprint arXiv:1107.4806*, 2011.

[35] R. Pesce. Energy calibration of data recorded with the surface detectors of the pierre auger observatory: an update. *Proc. 32nd ICRC, Beijing, China*, 2011.

[36] B.R. Dawsona et al. Proposal for an update of the auger energy scale. *Internal Auger Note,GAP-2012-124*, 2012.

[37] P. Abreu, M. Aglietta, M. Ahlers, E. J. Ahn, I. F. M. Albuquerque, D. Allard, I. Allekotte, J. Allen, P. Allison, A. Almela, et al. Search for point-like sources of ultra-high energy neutrinos at the pierre auger observatory and improved limit on the diffuse flux of tau neutrinos. *The Astrophysical Journal Letters*, 755(1):L4, 2012.

[38] Auger Collaboration. Interpretation of the depths of maximum of extensive air showers measured by the pierre auger observatory. *arXiv preprint arXiv:1301.6637*, 2013.

[39] K. H. Kampert and M. Unger. Measurements of the cosmic ray composition with air shower experiments. *Astroparticle Physics*, 35(10):660–678, 2012.

[40] P. Abreu, M. Aglietta, E. J. Ahn, I. F. M. Albuquerque, D. Allard, I. Allekotte, J. Allen, P. Allison, A. Almeda, J. Alvarez Castillo, et al. Measurement of the proton-air cross section at sqrt [s]= 57 tev with the pierre auger observatory. *Physical review letters*, 109(6):062002, 2012.

[41] T.K. Gaisser and A.M. Hillas. Reliability of the method of constant intensity cuts for reconstructing the average development of vertical showers. In *International Cosmic Ray Conference*, volume 8, pages 353–357, 1977.

[42] Henrique M.J. Barbosa, F. Catalani, J. A. Chinellato, and C. Dobrigkeit. Determination of the calorimetric energy in extensive air showers. *Astroparticle Physics*, 22(2):159–166, 2004.

[43] M. Unger, B. R. Dawson, R. Engel, F. Schüssler, and R. Ulrich. Reconstruction of longitudinal profiles of ultra-high energy cosmic ray showers from fluorescence and cherenkov light measurements. *Nuclear Instruments and Methods in Physics Research Section A: Accelerators, Spectrometers, Detectors and Associated Equipment*, 588(3):433–441, 2008.

[44] P. Hetzel. Untersuchungen zur unsichtbaren energie in ausgedehnten luftschauern. *http://www-ekp.physik.uni-karlsruhe.de/pub/web/thesis/iekp-bachelor-ka2012-9.pdf*.

[45] J. Linsley. Spectra, anisotropies and composition of cosmic rays above 1000 gev. In *International Cosmic Ray Conference*, volume 12, pages 135–191, 1983.

[46] M. Nyklíček and P. Trávníček. On the size of missing energy of cosmic ray showers. *icrc2009.uni.lodz.pl/proc/pdf/icrc0240.pdf*, ICRC Lodz 2009.

[47] A.G. Mariazzi and Collaboration Pierre Auger. A new method for determining the primary energy from the calorimetric energy of showers observed in hybrid mode on a shower-by-shower basis. *Arxiv preprint arXiv:1107.4804*, ICRC Beijing 2011.

[48] A.G. Mariazzi and M.J. Tueros. Estimating the missing energy of extensive air showers at the pierre auger observatory. *Internal Auger Note,GAP-2013-026*, 2013.

[49] J. Alvarez-Muniz, R. Engel, T. K. Gaisser, J. A. Ortiz, and T. Stanev. Hybrid simulations of extensive air showers. *Physical Review D*, 66(3):033011, 2002.

[50] J. Allen. Interpretation of the signals produced by showers from cosmic rays of 1019 ev observed in the surface detectors of the pierre auger observatory. *Proceedings of the 32nd ICRC, Beijing, China*, 2011.

[51] M. Ave, R. Engel, J. Gonzales, I.C. Maris, D. Maurel, and M. Roth. Number of muons from auger data. *Internal Auger Note,GAP-2011-090*, 2011.

[52] V. Verzi et al. Pierre auger collaboration meeting, malargue, argentina, 2013. *http://www.auger.org/admin/*.

Appendix

In this part, some figures or other details not necessary to follow the main body of the thesis can be found. We decided to add these parts into the Appendix because they can be useful in case of deeper interest in selected problems.

Simulation sets

The main simulation set consists of 13701 iron and 40407 proton showers simulated with hadronic model QGSJetII-03. Angle $(0° - 55°)$ and energy $(10^{16.5} - 10^{20.5}$ eV) distributions are continuous. Reconstruction was done with official software version Offline v7r6 for Infill array. In the table below, FD and SD cuts are specified.

Total events	54108
MinRecLevel	3
MaxZenithSD	55
T4Trigger	2
T5Trigger	2
SkipSaturated	(cut)
MaxCoreTankDist	750
EnergyError	0.2
XMaxError	40
ProfileChi2	2.5
DeltaProfileChi2	1.0
MaxDepthHole	30
XMaxObsInExpectedFOV	40 20
Selected events	17234

Four other simulation sets were used in this thesis. It was generated 200 showers for each of two models (QGSJetII-04 and EPOS LHC) and two primary particles (proton and iron). Zenith angle $(0° - 55°)$ and energy $(10^{17} - 10^{19}$ eV) with the spectrum slope index $(\alpha = 1)$ were continuously distributed. The detector response was simulated 10 times for every shower. The same cuts as for QGSJetII-03 (in the table above) were applied. After selection, it remained approximately 1000 showers for each primary particle and each model.

Data set

After more than 4 years of data taking, 406 golden hybrid events measured in Infill SD and FD (including HeCo) remained after high quality cuts (it the table below). 76 of them did not fulfill trigger efficiency condition and were left out for the final fit in the fourth chapter.

MinRecLevel	3
MaxZenithSD	55
T4Trigger	2
T5Trigger	2
LidarCloudRemoval	(cut)
hasMieDatabase	(cut)
maxVAOD	(cut)
skipSaturated	(cut)
badFDPeriodRejection	(cut)
MaxCoreTankDist	750
EnergyError	0.2
XMaxError	40
ProfileChi2	2.5
DeltaProfileChi2	1.0
MaxDepthHole	30
XMaxObsInExpectedFOV	40 20
Selected events	406

Estimation of the parameters $A(DX)$ and B

A fit with Eq. 4.1 in different DX bins is shown on Fig. 12.

Limitation of the estimation of $A(DX)$

A functional dependence of A on DX might seem at first sight as a third degree polynomial in the full DX range. The function $A(DX)$ is growing at higher DX (lower $X_{\max}$), when the signal S_{450} is smaller. At this point, we deal with a problem of trigger efficiency. This is illustrated in Fig. 13, where an additional condition (triggerefficiency > 0.99, as presented in section 2.2) was required and compared to a profile from all events. The difference expected at upper part of $A(DX)$ is present and this effect must be taken into a count. This trigger condition was added to the analysis in the last chapter.
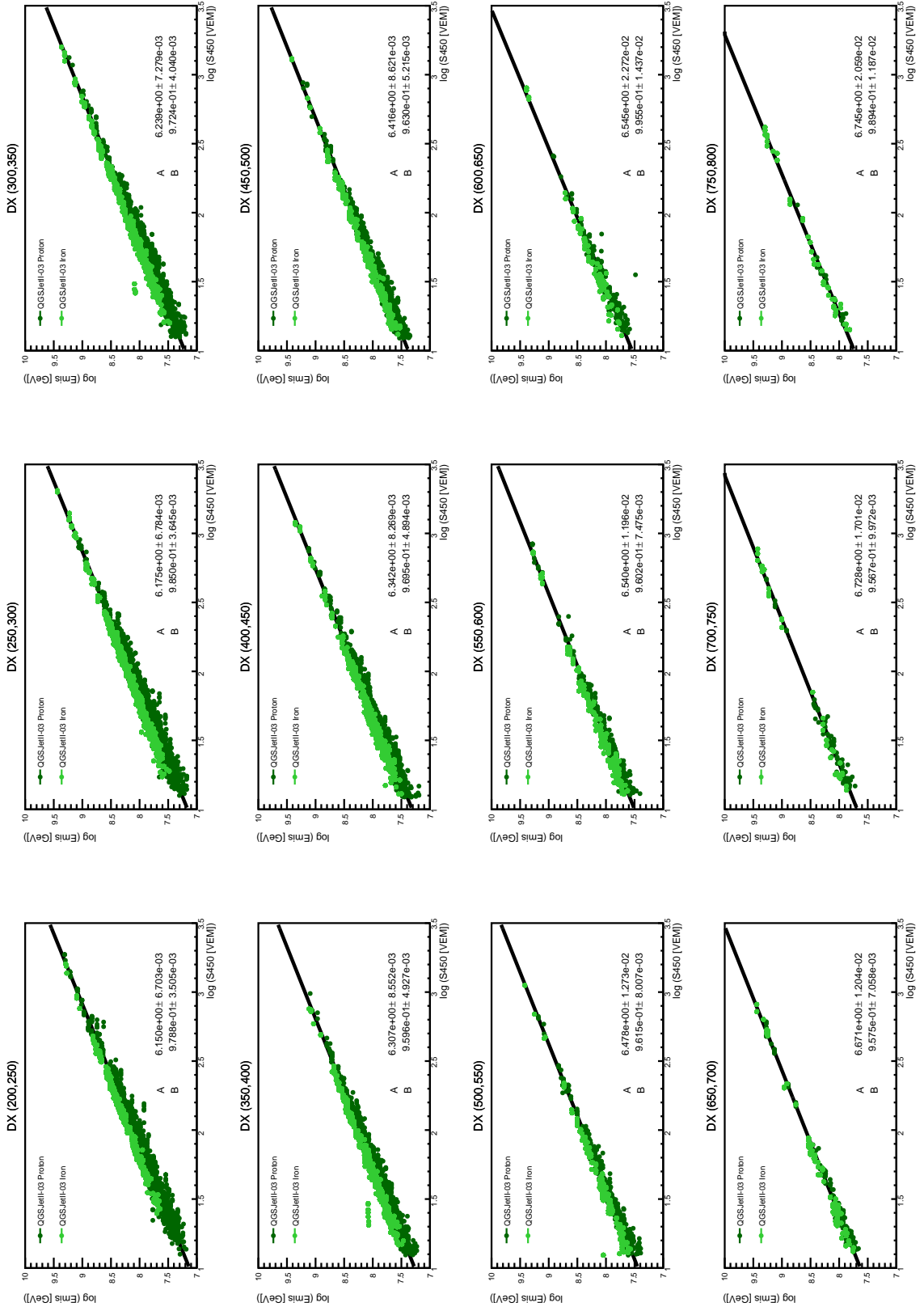
Figure 12: Dependence of the SD detector signal S_{450} [VEM] on the missing energy for different DX bins. E_{mis} [GeV] was computed as a difference between the energy of primary particle and the calorimetric energy, both taken from Monte Carlo informations about generated shower.
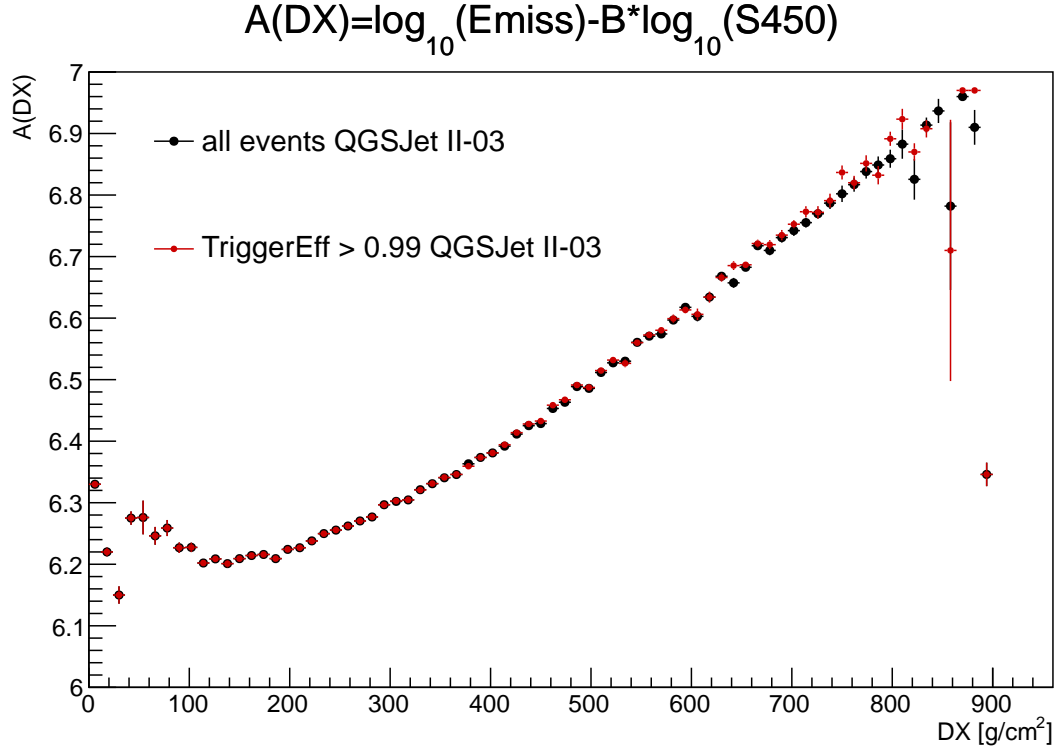
49

Figure 13: Profile of the function $A(DX)$ from all simulated events (black dots) compared with the profile, where the condition Trigger Efficiency > 0.99 was fulfilled (red dots).

On the other side, with decreasing DX we observe a saturation and minimum point, followed by a small increase of A. We expect here showers with high $X_{\max}$, these showers reach the maximum almost at the ground level and so at the limit of the detector. The saturation of the curve can by caused by this fact. An explanation of the rise of $A(DX)$ by the lowest DX is not that clear anymore. One possible reason for the grow can be a small contamination from electromagnetic particles by the showers with high zenith angle and consequently bigger part of the missing energy is present. This was researched on the Fig. 14, where the parameter $A(DX)$ is plotted in different zenith angle Θ bins. The same plots additionally divided in energy bins are shown on Fig. 17.

A hypothesis that the shape of the curve $A(DX)$ is influenced by selection of the events (FD cuts) was disproved. Function $A(DX)$ from the events without FD cuts shows the same behavior as $A(DX)$. This crosscheck is illustrated on the Fig. 15.

Another reason can be simply an effect of parametrization. Equation 3.7 was replaced by

$$E = \gamma_o(X_{\max})S_{35}^{\gamma}. \tag{8}$$

Parameter A can be expressed as a function of $X_{\max}$, the zenith angle dependence is hidden in CIC[1] and we use $S_{35} = S_{450}/\text{CIC}$ instead of S_{450}. Function $A(X_{\max})$ shows the same behavior as $A(DX)$ and so another assumption was disproved. $A(X_{\max})$ (from the events without FD cuts) is illustrated on the Fig. 16. The same plots

---

[1]Constant intensity cut $\text{CIC}(x) = 1 + bx + cx^2 + dx^3$ with $x = \cos^2(\Theta) - \cos^2(35)$ and values $b = 1.688761, c = -1.285305, d = -2.302623$ were taken.
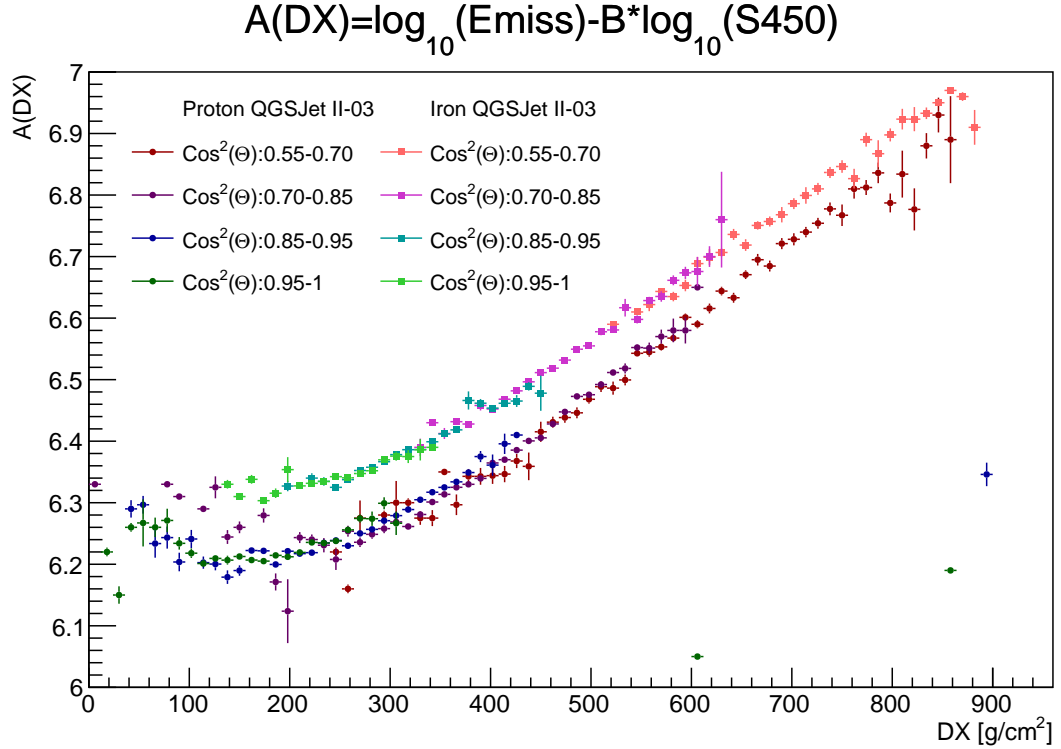
Figure 14: Parameter A depending on DX in different zenith angle Θ bins separately for proton and iron showers.

additionally divided in S_{35} bins can be found in Fig. 18. We decided to use for the parametrization the function $A(DX)$ and not $A(X_{\max})$ because it disposes of a smaller spread between proton and iron showers.

We investigated to divide the function $A(DX)$ into a two parts and fit them separately. For the interval $DX = 0 - 280$, the parabola function $f(DX) = a + b \cdot DX + c \cdot DX^2$ was applied and for $DX = 280 - 850$ a simple linear function $g(DX) = d + e \cdot DX$ was selected. Two additional conditions were acquired, in order to get continuous function: $f(280) = g(280)$ and $f'(280) = g'(280)$. The resulting function combined from these two parts has three parameters. This was compared to third degree polynomial fit in in whole range of DX. None of the parametrisations described sufficiently the feature at the low DX. The curvature is very probably caused by the limitation of the detector and we decided to fit $A(DX)$ in the range $DX = 200 - 850$ g/cm^2.

Parametrisation of the missing energy from data

For the computation of the correction factor from the Eq. 4.6 we need values of γ_0^{mc} and γ_0^{data}. Fits of the attenuation curve for simulated events in different DX bins are on Fig. 19 and for measured events on Fig. 20.
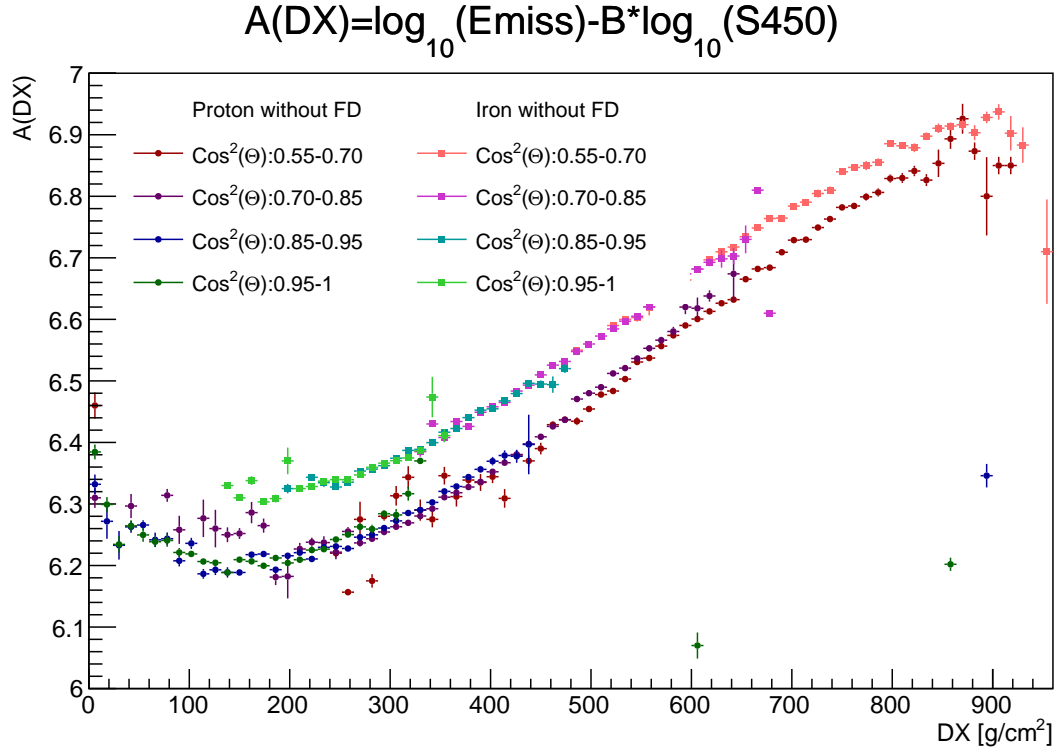
A(DX)=log₁₀(Emiss)-B*log₁₀(S450)

Figure 15: Parameter A depending on DX in different zenith angle Θ bins separately for proton and iron showers from simulations without FD cuts.
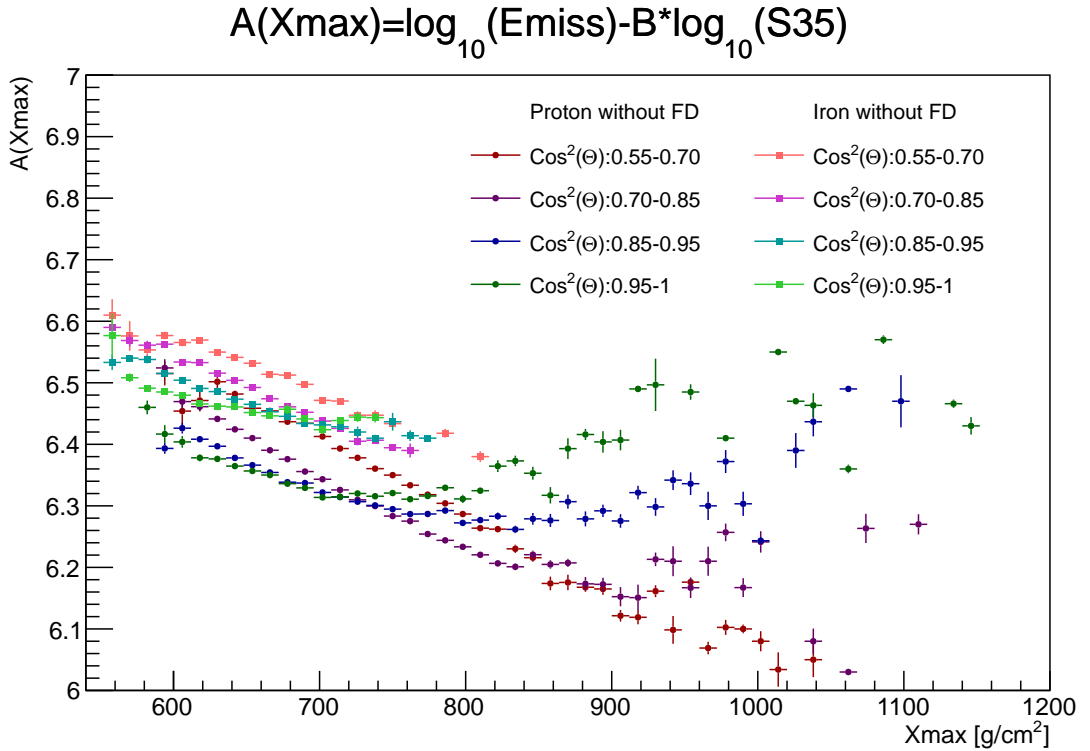
A(Xmax)=log₁₀(Emiss)-B*log₁₀(S35)

Figure 16: Parameter A depending on $X_{\max}$ in different zenith angle Θ bins separately for proton and iron showers. Instead of S_{450} was taken signal at the 450 m from the shower core divided by constant intensity cut $S_{35} = S_{450}/CIC$.
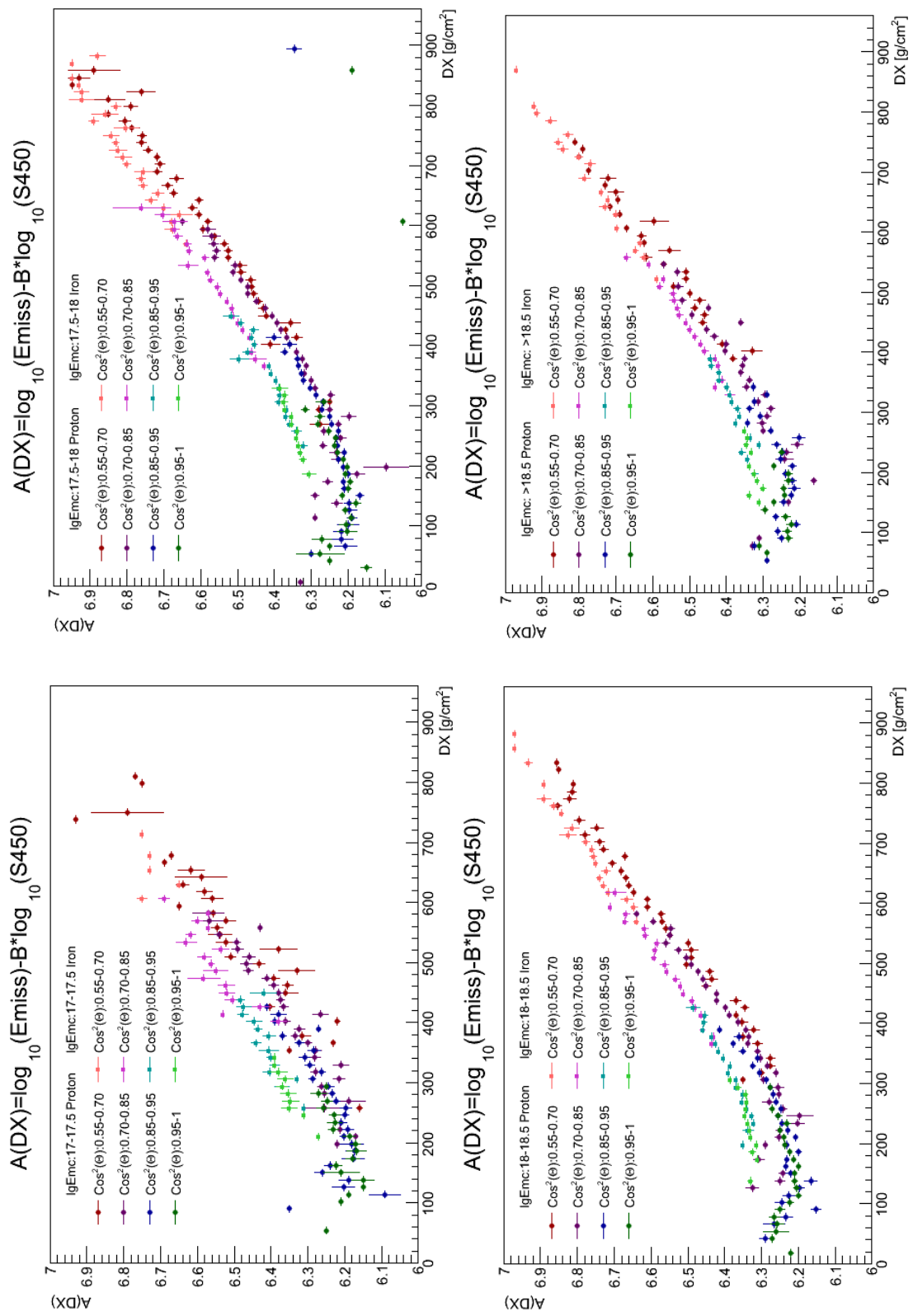
Figure 17: Parameter A depending on DX in different zenith angle Θ bins separately for proton and iron showers, each figure represents different energy bin.
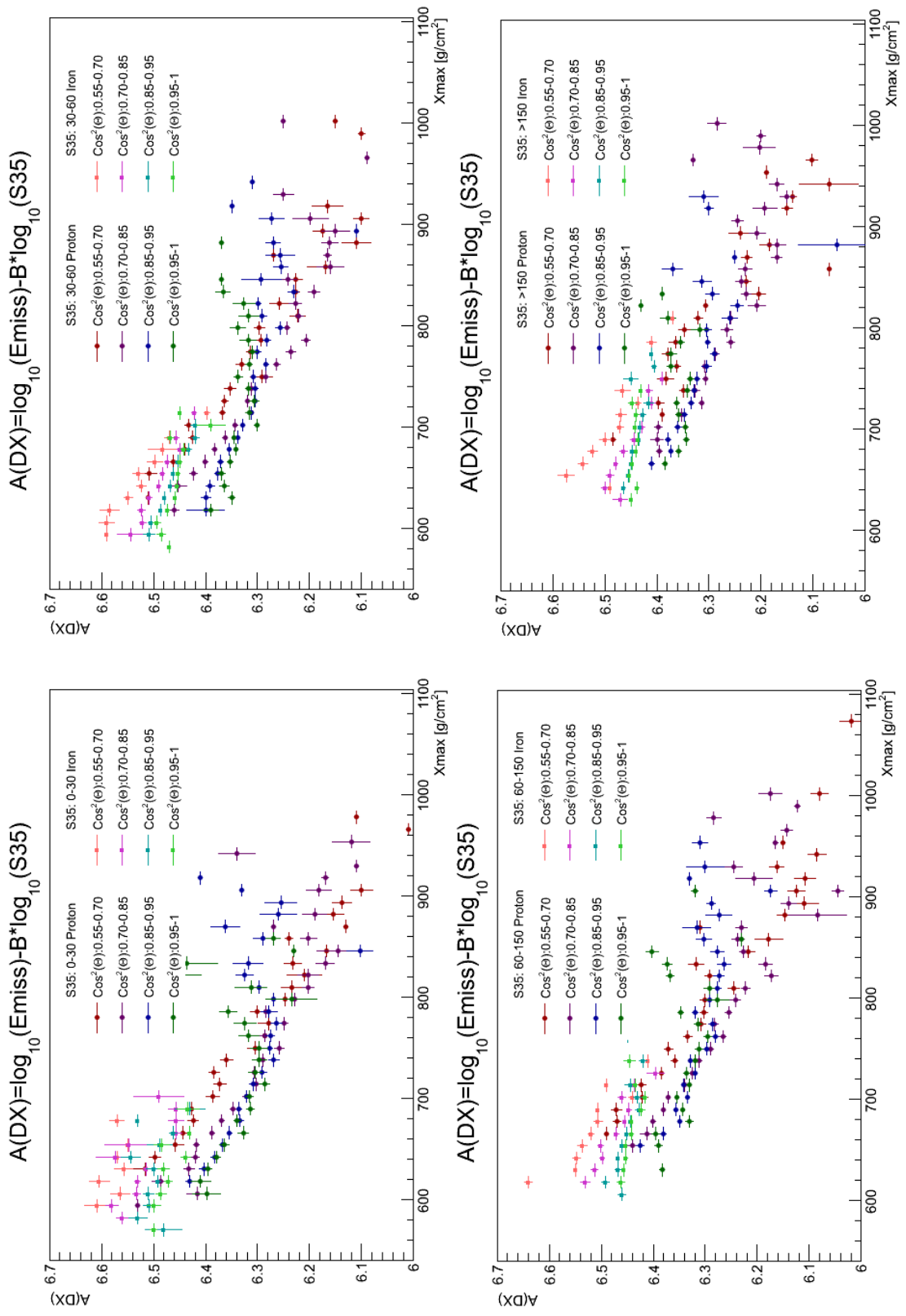
Figure 18: Parameter A depending on $X_{\max}$ in different zenith angle Θ bins separately for proton and iron showers from simulations without FD cuts. Instead of S_{450} was taken signal at the 450 m from the shower core divided by constant intensity cut $S_{35} = S_{450}/CIC$. Every figure represents different S_{35} bin.
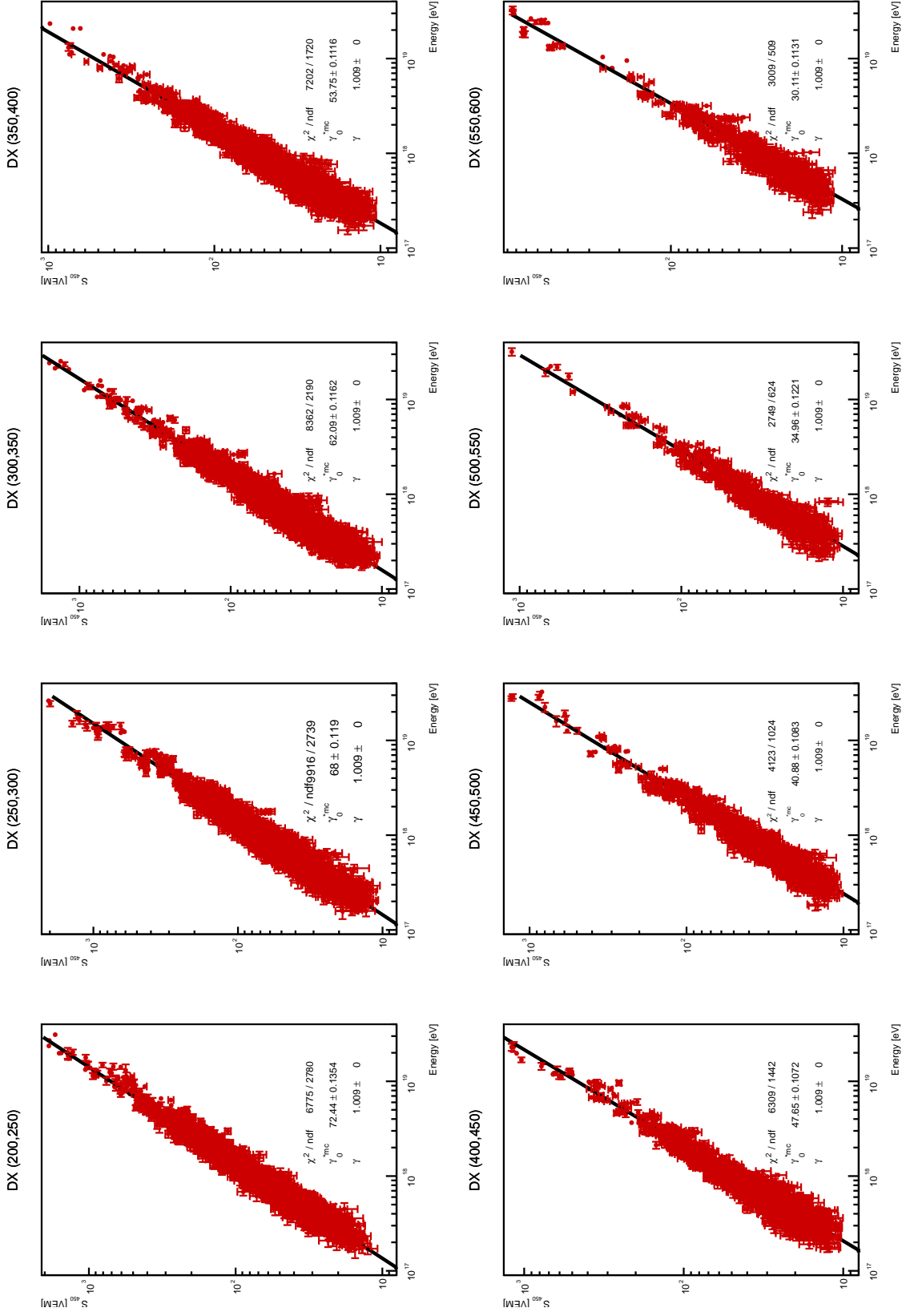
Figure 19: Estimation of the parameter γ_0^{mc} from the fit $S_{450} = \gamma_0(E/10^{18})\gamma$ to data simulated with QGSJetII-03 in different DX bins.
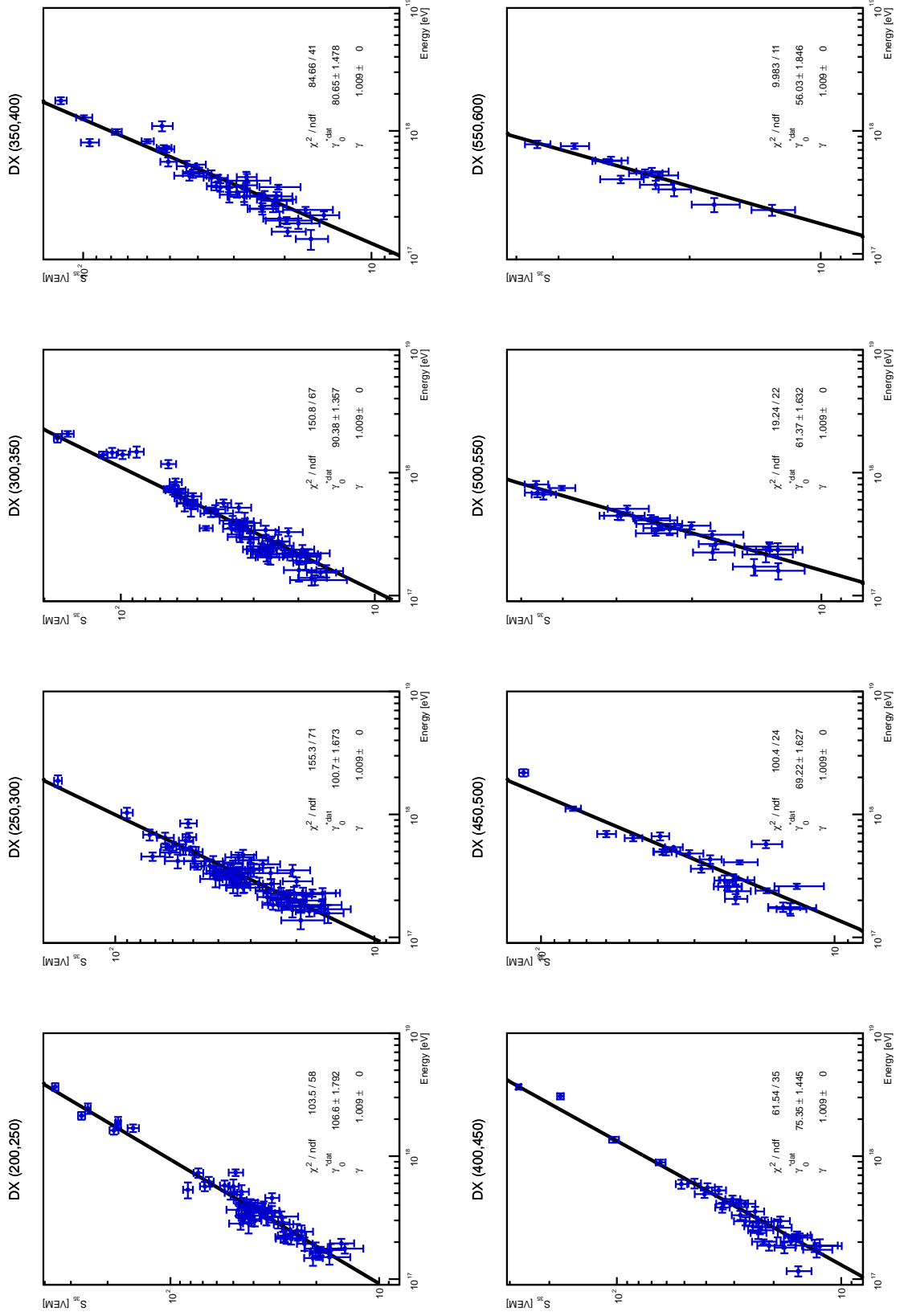
Figure 20: Estimation of the parameter γ_0^{data} from the fit $S_{450} = \gamma_0 (E/10^{18})^\gamma$ to measured HeCo data in different DX bins.